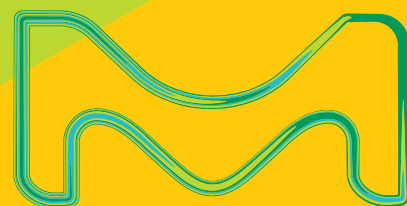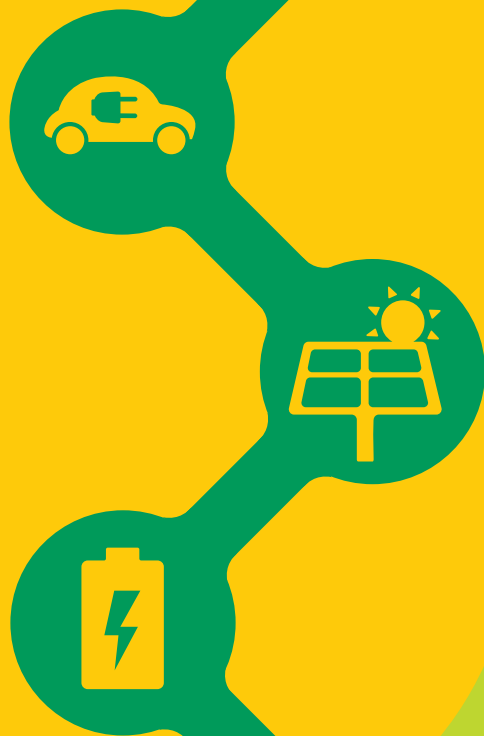# Material Matters™

Batteries & Solar Cells

Production of Nickel-Rich Layered Cathode Materials for High-Energy Lithium-Ion Batteries via a Couette-Taylor-Flow-Reactor

Advancements in Quantum Dot Solar Cells: Synthesis and Applications

Advances in Conversion-Type Li-Metal Fluoride Battery: A Mini-Review

Recent Trends in Perovskite Solar Cells

Recent Advances in Solid-State Rechargeable Batteries

Introduction

Megan Muroski, Ph.D
Global Product Manager - Nano-materials and Energy

Welcome to the second issue of *Material Matters*™ in 2020, focusing on battery and solar energy materials. This issue highlights recent trends associated with new material discoveries related to perovskites, solar cells, and battery advances.

In our first article, researchers from the Münster Electrochemical Energy Technology Battery Research Center, Dr. Schmuch, Dr. Siozios, Professor Dr. Winter, and **Dr. Placke** review the challenges and opportunities of nickel-rich layered oxide cathode materials. In this article, the authors discuss production processes for the layered oxide cathode materials as well as their chemistry and morphology. The researchers also discuss the synthesis of these materials using a continuous Couette-Taylor Flow reactor, which results in highly uniform particles and short residence times.

In their article focused on advancements in quantum dot solar cells, **Professor Sharma** and colleagues (Council of Scientific & Industrial Research, India) review the synthesis and applications of this novel material. This includes a discussion of the unique properties of quantum dots and their suitability for solar cell applications, along with common synthesis techniques used to develop these materials. They further review different classifications of semiconductor quantum dots with a description of commonly used materials and their advantages and disadvantages. Also, the researchers discuss the future scope and challenges ahead for these materials.

Our next article from **Professor Qiao's** laboratory (South Dakota State University, USA) lays out recent advances in conversion type lithium metal fluoride batteries. This review explores key concepts in developing electrochemically stable microstructures for wide Li-ion insertion channels. Furthermore, this article goes through the development of electrolytes, and discusses the concentration, additives, and solid electrode interfaces to stabilize the Li metal anode. In addition, the authors highlight the optimization and modification of battery components to improve the performance of Li-metal fluoride batteries.

In our fourth article, **Dr. Perini and Professor Correa-Baena** discuss the latest research and effort to obtain higher performance and stability of perovskite materials. In this article, they discuss the state of the art of device structures and lead halide perovskites, including examining compositional engineering, halide segregation, and black phase stabilization. Finally, they discuss perovskite solar cell stability, aging protocols, field testing and other remaining challenges.

In our final article, **Dr. Sun** from the Beijing Institute of Nanoenergy and Nanosystems reviews the recent advances in solid-state rechargeable batteries. This review covers the fundamentals of solid electrolytes in solid-state batteries, the theory of ion conduction, and the structures and electrochemical processes of solid-state Li batteries. Sodium and Aluminum solid-state batteries and the progress and perspectives of these materials are also highlighted.

Each article in this publication concludes with a list of relevant Sigma-Aldrich materials available from Merck. For additional product information, please visit us at **SigmaAldrich.com/matsci**. If you have any new product suggestions, questions or comments, or new ideas for future *Material Matters*™ issues, please contact us at **SigmaAldrich.com/technicalservice**.

About the Cover

In addition to contributing to environmental benefits, new approaches to alternative energy harvesting and storage, are imperative to meet future energy demands. The solar panels and energy storage device on the cover art depicts the importance of both energy harvesting and storage. The flower represents the synergy of both approaches for a better environment. For these technological areas to blossom, cutting edge ideas will be required to expand the roots of knowledge, including the development of novel materials. The Sigma-Aldrich® portfolio of Materials Science products enables alternative energy and storage technologies with an extensive portfolio of materials to help researchers grow their seeds of knowledge.

Table of Contents

Articles

Featured Products

Your Material Matters

Bryce P. Nelson, Ph.D.
Materials Science Initiative Lead

The development of 2D van der Waals materials that expand beyond graphene is an area of great interest due to their applications in optoelectronic applications, including photodetectors and solar cells. Germanane is a germanium graphene analog, with a direct bandgap of 1.6 eV and electron mobility of 18000 cm^{2}V^{-1}s^{-1}. We offer hydrogen-terminated germanium (Ge, **906026**), which is synthesized by the topotactic deintercalation of CaGe$_2$ crystals. Its crystal structure contains a hexagonal Ge lattice containing covalently attached hydrogen atoms.

In collaboration with Professor Joshua Goldberger at Ohio State University, we recently developed several Germanane analogs with tunable electronic properties. Germananes exhibit semiconducting properties with a direct bandgap of 1.50 eV. Also, they have high electron mobility, and its alkylation allows bandgap tuning from 1.50 eV for allyl (**910988**) to 1.62 eV for methyl germanane (**909114**). The unique properties of these materials make them useful in a wide range of applications, including energy storage and semiconducting properties, providing exciting alternatives to current 2D material technologies.

References
(1) Jiang, S; Bianco, E.; Goldberger, J. E. *J. Mater. Chem. C* **2014**, *2* (17), 3185–3188.
(2) Madhushankar, B. N.; Kaverzin, A.; Giousis, T.; Potsi, G.; Gournis, D.; Rudolf, P.; Blake, G. R.; van der Wal, C. H.; van Wess, B. J. *2D Mater.* **2017**, *4* (2), 021009–021009.
(3) Serino, A. C.; Ko, J. S.; Yeung, M. T.; Schwartz, J. J.; Kang, C. B.; Tolbert, S. H.; Kanner, R. B.; Dunn, B. S. Weiss, P. S. *ACS Nano* **2017**, *11* (8), 7995–8001. DOI: 10.1021/acsnano.7b02589

Name	Cat. No.
Germanane	**906026-1G**
Methyl germanane	**909114-1G**
Allyl germanane	**910988-1G**
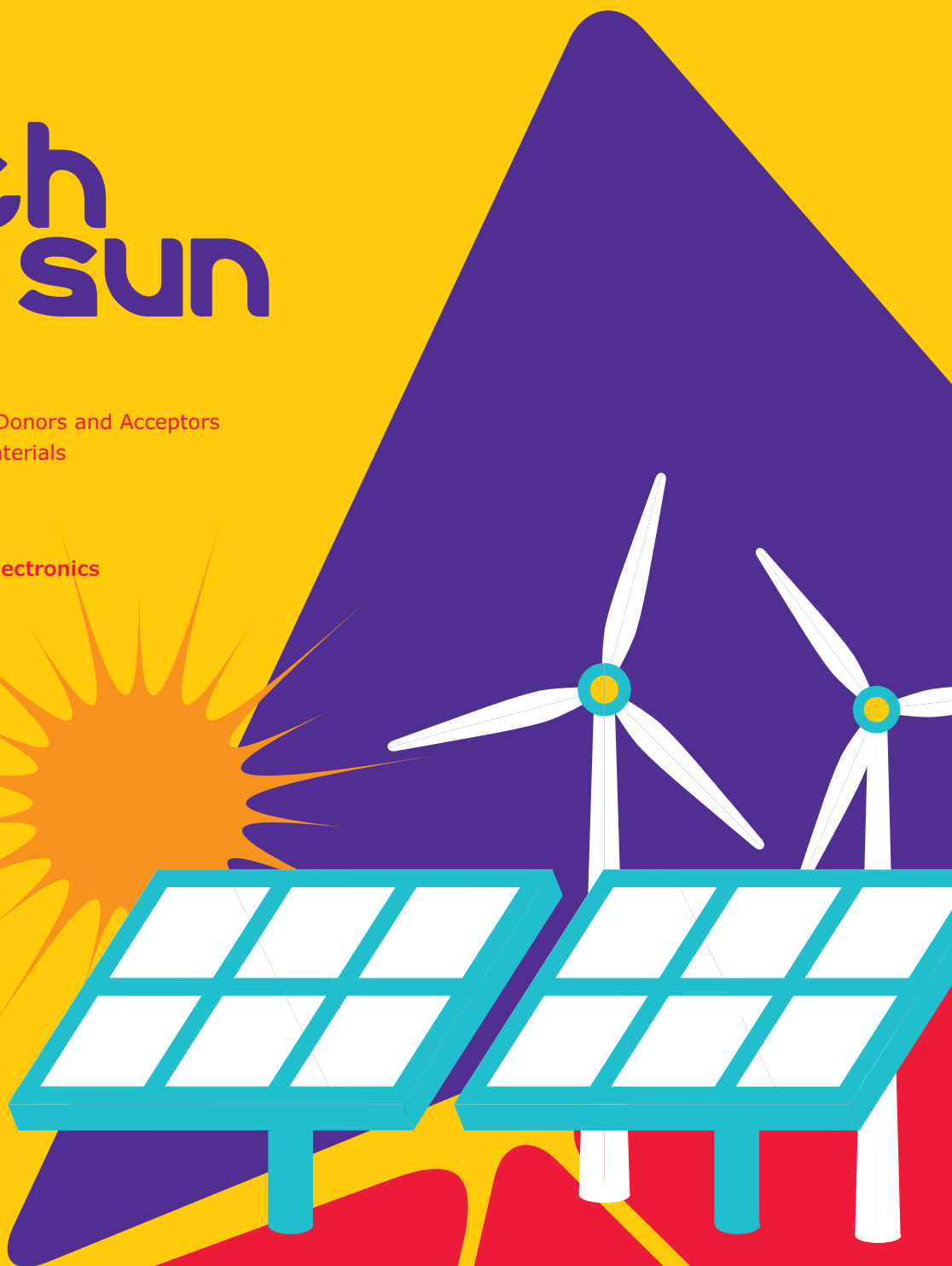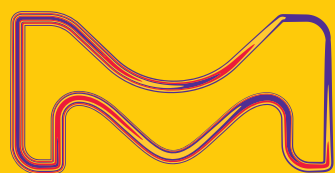
Production of Nickel-Rich Layered Cathode Materials for High-Energy Lithium Ion Batteries via a Couette-Taylor-Flow-Reactor

Richard Schmuch,[1]* Vassilios Siozios,[1] Martin Winter,[1,2] and Tobias Placke[1]

[1] University of Münster, MEET Battery Research Center, Institute of Physical Chemistry, Corrensstr. 46, 48149 Münster, Germany
[2] Helmholtz Institute Münster, IEK-12, Forschungszentrum Jülich GmbH, Corrensstr. 46, 48149 Münster, Germany
* Email: richard.schmuch@uni-muenster.de

Introduction

Lithium ion batteries (LIBs) are the state-of-the-art rechargeable electrochemical power source that currently dominates high energy density applications such as portable electronic devices and electromobility.[1–3] To enable faster and more extensive market penetration of electric vehicles (EVs), the industry must achieve driving ranges of at least 500 km at an affordable cost. However, achieving such a feat requires further innovation to improve efficiency by increasing energy density (>500 Wh L^{-1}) and reducing cost (<125 US\$ kWh^{-1}) at the battery pack level.[2] Despite further possible optimizations of the LIB cell and pack design (e.g., cell design and housing, cooling system), the development of advanced LIB cell chemistries will have a significant impact on energy content and cost savings.[2,4,5]

Challenges and Opportunities for Nickel-rich Layered Oxide Cathode Materials

Over the last decade, the establishment of state-of-the-art positive electrode (cathode) materials in high-energy LIB cells has come as a result of advancements in nickel (Ni)-containing $LiMO_2$-type layered oxides (where M denotes metals such as Ni, Co, Mn, Al, etc).[2,5,6] In particular, these polyatomic compounds appear as variations of $Li[Ni_xCo_yMn_z]O_2$ ($x+y+z = 1$; NCMxyz) and $Li[Ni_{1-x-y}Co_xAl_y]O_2$ (NCA).

Two major strategies are currently employed to increase the energy content of advanced cathodes to target values of ≥800 Wh kg^{-1} and ≥4,000 Wh L^{-1}. The first approach is to increase the Ni-content of the layered oxides (≥80%) to enhance specific cathode capacity; the second strategy is to increase the charging cut-off potential (e.g., >4.3 V vs. Li|Li$^+$) of lower Ni (≤60%) cathode formulations.[5,7] Lately, LIB cells based on NCM811 (e.g., pouch format cells by CATL Battery) and NCA chemistries (21700 cylindrical format cells by *Panasonic*), having Ni-contents of ~≥80% and exhibiting 80–100 g Co per kWh and <50 g Co per kWh, respectively, have already entered the EV market.[5] Besides energy density improvements, a major driving force for further cathode material development is to lower the cobalt (Co) content of the cathode, a scarce and costly element. Cobalt mining primarily occurs in politically unstable regions in Central Africa, involving severe environmental pollution as well as widespread allegations of extraction by child labor.[2,5] For this reason, the scientific community has invested heavily in research to develop Co-free or low-Co Ni-rich, layered oxide cathode materials.[8,9]

However, both of the previously mentioned strategies result in severe challenges concerning the cathodes' cycle life and thermal stability (safety). These two features often present hurdles due to the limited structural stability upon excessive de-lithiation, involving multiple phase transformations of both bulk (i.e., lithium ordering) and particle surface (i.e., layered to rock salt formation), especially for Ni-rich cathode compositions.[5] Further challenges include parasitic side reactions, such as electrolyte oxidation accompanied by gas evolution, transition
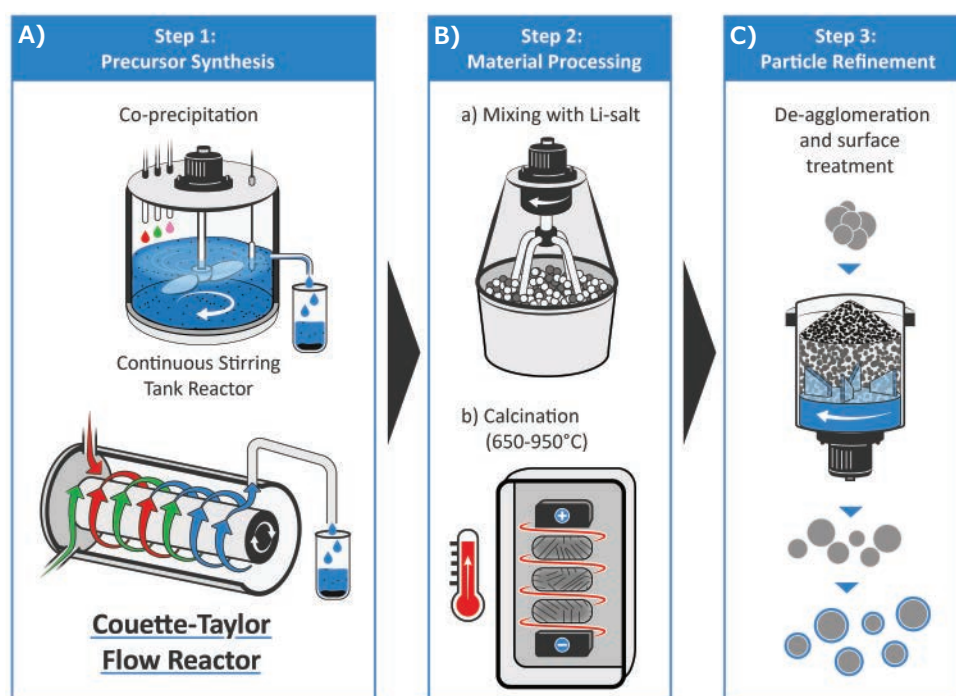
Figure 1. Schematic illustration of the production process for layered oxide cathode materials for LIB cells. **A**) Step 1: Precursor synthesis via co-precipitation in a CSTR or CTFR, followed by post-particle treatments (filtration, washing, drying, sieving). **B**) Step 2: Lithiation via mixing with a lithium salt (LiOH or Li_2CO_3) and calcination (650–950 °C). **C**) Step 3: Particle refinement procedures by de-agglomeration of particles and surface treatment (like post-calcination, etc.).

metal dissolution and cross-talk phenomena, and as well as particle (micro)-cracking by anisotropic lattice distortion.[5,7,10,11]

Besides chemistry, the electrochemical performance of cathode materials also depends on their particle properties, such as morphology and microstructure (size and shape of primary particles and their alignment within the secondary particle), size distribution, tap density, specific surface area, and surface characteristics.[5] Thus, tailored particle engineering of layered cathode materials during synthesis allows for an achievable optimum energy output while still addressing cycle life and thermal stability aspects via particle refinement strategies.

Production Processes for Nickel-Rich Layered Oxide Cathode Materials

Figure 1 illustrates the three critical steps of the production process of $LiMO_2$-type layered oxide cathode materials, (A) precursor synthesis, (B) material processing, which includes precursor lithiation and calcination, and (C) particle refinement.[2,5] The precursor materials are typically prepared via an aqueous co-precipitation route in a batch reactor, in a continuously stirred tank reactor (CSTR), or a Couette-Taylor-Flow-Reactor (CTFR), which are introduced later in this work.[12,13]

The careful adjustment of each production step and multiple synthesis parameters is required to obtain the required cathode particles with tailored characteristics. Various studies have suggested that precursors significantly affect the properties of cathode materials through their chemical composition, particle morphology, and size distribution.[5,12,14] Therefore,

systematic studies in terms of optimum synthesis parameters for co-precipitation are mandatory, e.g., by adjusting the pH value, amount of ammonia concentration, and the type of base (hydroxide vs. carbonate). Furthermore, the lithiation/calcination process requires optimization concerning its conditions (e.g., LiOH vs. Li_2CO_3, calcination temperature, air vs. O_2 atmosphere), while the post-treatment for Ni-rich materials typically necessitates a high corrosion resistance of the used equipment as well as a strict humidity control.[5]

It is well known that the particle properties of the NCM precursor materials strongly depend on the crystal agglomeration mechanism. This feature occurs via consecutive steps of physical adhesion of the crystals forming aggregates, followed by aggregate growth.[15] The agglomeration process is complex and depends on various synthesis conditions. These conditions include the type and layout of the reactor, determining the fluid motion (e.g., turbulent vs. laminar) and, thus, the particle collisions resulting in agglomeration.[15] Two types of chemical reactors, batch reactors, and CSTRs are widely adopted for precursor material preparation.[13] A third reactor, the CTFR — also known as Taylor vortex reactor (TVR), is currently being reviewed to provide improved mixing of the reactants (**Figure 1A**).[13,15-19] The co-precipitation route within batch or CSTR processes are commercially applied for the NCM precursor production, due to its advantages for achieving particles having a homogeneous composition, narrow size distribution and high tap density.[12,20] However, these two production routes also suffer from shortcomings, such as typically long reaction times (~15–25 h), process complexity for CSTR operation as well as possible

batch-to-batch variability and labor-intensive operation for batch processes.[13] In this respect, process development and scale-up of cathode material synthesis towards larger batch sizes (≥1 kg; e.g., by continuous processes) are a critical bridge between fundamental laboratory research, prototype development for validation, and high-volume production.[20]

Production Detail for Nickel-Rich Layered Oxide Cathode Materials

To prepare an NCM811 precursor ($Ni_{0.8}Co_{0.1}Mn_{0.1}(OH)_2$) as in the first step of **Figure 1A**, feed 1.5 molar aqueous solutions of the divalent transition metal salts, nickel sulfate hexahydrate ($NiSO_4 \cdot 6H_2O$, **Cat. No. 227676**), cobalt sulfate heptahydrate ($CoSO_4 \cdot 7H_2O$, **Cat. No. C6768**), and manganese sulfate monohydrate ($MnSO_4 \cdot H_2O$, **Cat. No. M7634**) into the reactor. Simultaneously a 3.0 molar aqueous base solution of sodium hydroxide (NaOH, **Cat. No. 567530**) and chelating agent of ammonium hydroxide (12 wt.% NH_4OH, **Cat. No. 338818**) is pumped into the reactor under pH (~12) and temperature control (~60 °C), causing the metal hydroxide ($M(OH)_2$) precursor precipitates.

Afterward, the obtained precursor requires filtration and repeated washing to remove impurities (i.e., sodium and sulfate ions), followed by drying and (optional) sieving to adjust to a particular particle size distribution. In the second step (**Figure 1B**), mix the precursor particles with a stoichiometric amount of a lithium-containing salt, i.e., lithium hydroxide monohydrate ($LiOH \cdot H_2O$, **Cat. No. 402974**) or lithium carbonate (Li_2CO_3, **Cat. No. 601470**), and calcine in a temperature range between ~650–950 °C in oxygen atmosphere.[2,5] Even though Li_2CO_3 has a lower cost, Ni-rich cathodes are known to have more favorable particle and electrochemical characteristics when calcined with LiOH.[2,5] The final step (**Figure 1C**) requires particle refinement approaches, such as de-agglomeration, purification, drying and sieving, as well as surface treatments, e.g., post-calcination, to stabilize the cathode material interface.[2,5]

Cathode Material Synthesis via a Continuous Couette-Taylor Flow Reactor

For electric vehicle (EV) applications, the volumetric energy density (Wh L[-1]) of battery materials and the resulting cells are broadly seen as more important than specific energy (Wh kg^{-1}). Consequently, the cell requires fabrication of composite electrodes with high areal capacities >3–4 mAh cm^{-2} and pressed electrode densities of 3.0–3.4 g cm^{-3}.[5] Scientists can achieve a high electrode density by using cathode materials with high crystallographic density (>4 g cm^{-3}), large particle size (≥10 µm), and bimodal size distribution; however, a spherical particle morphology reduces slurry viscosity and improves packing density.[5,21] The CTFR has recently emerged as a popular reactor type for the continuous production of cathode precursors.[13,15,17–19] The CTFR conveys numerous advantages over established CSTR and batch processes, such as allowing

very homogeneous micro-mixing with higher mixing intensity, shorter processing times, design of dense particles by fast reaction kinetics, and design of highly uniform spherical particles with narrow size distribution.

Figure 2 shows the setup and operating principle of a CTFR (LCTR®-Tera 3300, Laminar). The reaction tube of the CTFR consists of two coaxially arranged cylinders with a narrow reaction zone (6.55 mm) in between, as illustrated in **Figure 2A**. Upon operation, the inner cylinder rotates, inducing a stable Taylor-vortex flow pattern above a threshold rotational speed. The confined Taylor vortices increase the shear forces in the reaction mixture, promoting the agglomeration of spherical precipitates with a narrow particle size distribution (**Figure 2B**).[15,18,19,22]

The Taylor-vortex flow patterns form above the critical Taylor number (Ta), as shown in equation (1), in which d is the gap of the cylinders, r_i is the radius of the inner cylinder, ω_i is the rotational angular speed, and v is the viscosity of the fluid.[15-16,23]

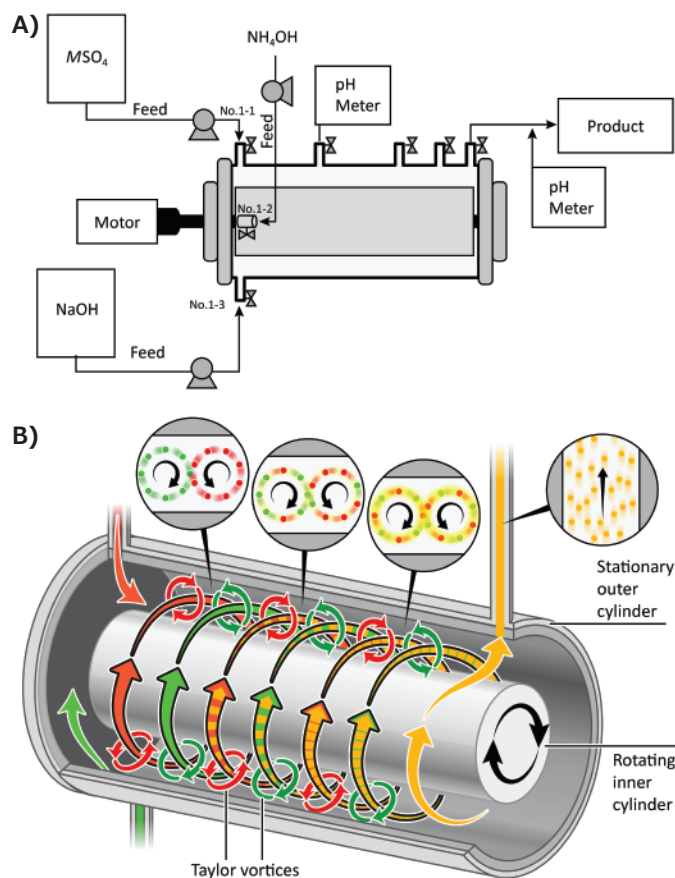$$Ta = \frac{\omega_i\, r_i\, d}{v} \sqrt{\left(\frac{d}{r_i}\right)} \tag{1}$$

Figure 2. Schematic illustration of **A**) the experimental setup for co-precipitation of metal hydroxides in a continuous CTFR and **B**) Taylor vortex flow patterns induced along the reaction tube of the CTFR. Adapted with permission from references 15 and 18, 2011 Elsevier and 2015 ACS Publications (respectively).

Figure 3. SEM images of $Ni_{0.8}Co_{0.1}Mn_{0.1}(OH)_2$ precursor materials synthesized via the CTFR (pH value: 12; T: 60 °C; τ: 4 h) showing the dependence of the rotational speed (ω_i) of the inner cylinder. **A)** ω_i: 500 rpm; **B)** ω_i: 900 rpm; **C)** ω_i: 1300 rpm.

Obtaining precursor materials with optimized particle characteristics requires scientists' careful evaluation and selection of various CTFR parameters. Adjustable parameters for the co-precipitation process include synthesis temperature (T), mean residence time (τ), pH value, concentrations of the reactant solutions, as well as the rotational speed (ω_i) of the inner cylinder. For the production of hydroxide precursors ($Ni_{0.8}Co_{0.1}Mn_{0.1}(OH)_2$), the operation temperature was set to ~60 °C and the pH value was adjusted to ~12. **Figure 3** and

Figure 4 show the impact of varying rotational speeds (500, 900, and 1300 rpm; τ : 4 h) on the resulting particle morphology and particle size distribution.

One can observe that the obtained NCM811 precursor materials display a bimodal particle size with a narrow size distribution (**Figure 4A**). Additionally, the rotational speed significantly influences the particle size, which increases with decreasing ω_i, as depicted by the average D90 and D_{mean} values (**Figure 4B**). The tap density of the precursor materials (~1.6 g cm^{-3}) is nearly independent of the changes in particle size. Furthermore, one can recognize the more uniform spherical particles obtained at moderate or low rotational speeds (≤900 rpm, **Figure 3**).

In the next step of cathode material production, scientists lithiated the precursor materials by mixing them with $LiOH \cdot H_2O$ and subsequent calcination (800 °C, 10 h, O_2 atmosphere). In an exemplary result, **Figure 5** displays the comparison of the

Figure 4. Particle size distribution of $Ni_{0.8}Co_{0.1}Mn_{0.1}(OH)_2$ precursor materials synthesized via the CTFR (pH value: 12; T: 60 °C; τ: 4 h; ω_i: 500-1300 rpm). **A)** Cumulative values and density distribution; **B)** Average values of D90 and mean particle size distributions.

Figure 5. SEM images of the **A)** precursor material $Ni_{0.8}Co_{0.1}Mn_{0.1}(OH)_2$ synthesized via the CTFR (pH value: 12; T: 60 °C; τ: 2 h; ω_i: 500 rpm) and **B)** the lithiated $Ni_{0.8}Co_{0.1}Mn_{0.1}O_2$ material obtained via lithiation using LiOH (calcination at 800 °C for 10 h, O_2 atmosphere).

Figure 6. Charge/discharge cycling performance of NCM811||graphite full-cells (two-electrode setup; CR2032 coin cells). Cycling conditions: Cell voltage range of 2.8-4.3 V; 3 formation cycles at 0.1C, followed by cycling at 0.5C (1C=200 mA g^{-1}) with 0.1C cycling steps after each 100 cycles. Positive electrode: NCM811:PVdF binder:Super C65 = 92:4:4; areal capacity: 2.0 mAh cm^{-2}; graphite negative electrode: 2.6 mAh cm^{-2}; Electrolyte: 1M LiPF$_6$ in ethylene carbonate (EC)/diethyl carbonate (DEC) (3:7 by weight).

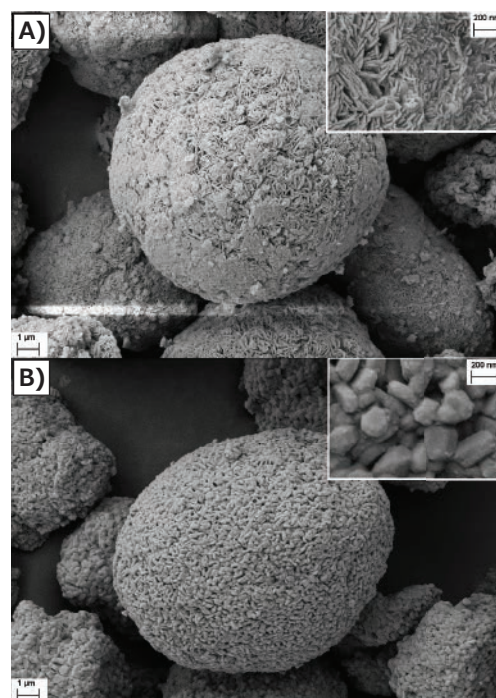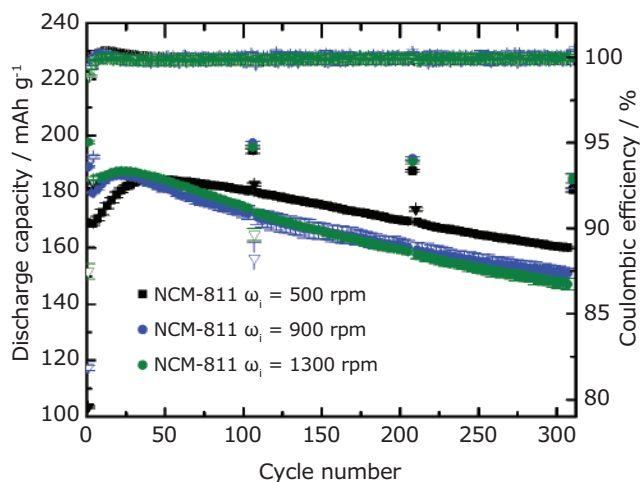particle morphology for an NCM precursor particle (**Figure 5A**) and a lithiated NCM811 particle (**Figure 5B**). One can see that the nanosized primary particles of the precursor become larger primary particles for NCM811 during the calcination step at 800 °C (**Figure 5B**). The tap density for the NCM811 materials ranges from ~1.5–2.0 g cm^{-3}, depending on the rotational speed (500–1300 rpm). Furthermore, one can observe a change of the BET specific surface area (~0.6–1.5 m^2 g^{-1}), which correlates well with the changes in the particle size distribution, i.e., a decrease of the average particle size results in an increase of the specific surface area.

Figure 6 presents the long-term charge/discharge cycling performance of NCM811 || graphite LIB full-cells for three different NCM811 materials, i.e., for precursor materials obtained at different rotational speeds (pH value: 12; *T*: 60 °C; *τ*: 2 h; ω$_i$: 500, 900 and 1300 rpm). From the figure, it can be observed that the particle characteristics have a significant impact on the electrochemical performance of the full-cells. For instance, the larger NCM811 particles (ω$_i$: 500 rpm) display a lower 1st-cycle Coulombic efficiency and lower initial capacity but higher capacity retention. In contrast, the smaller particles (ω$_i$: 900 and 1300 rpm) exhibit a higher 1st cycle Coulombic efficiency and higher initial capacity, while the capacity retention is inferior compared to larger particles. Future systematic studies in terms of material design and electrochemical performance analysis are mandatory to validate structure-performance correlations.

Summary

The cathode is the decisive cell material for further increasing energy content and lowering the costs of future advanced LIB cells; cathode chemistry and morphology both contribute equally to achieving these goals. The CTFR is a powerful reactor type for the continuous co-precipitation of spherical precursors for Ni-rich layered cathode materials, enabling the synthesis of highly uniform particles under relatively short residence times. Scientists can adjust particle characteristics such as particle morphology and size distribution, by choosing suitable synthesis parameters including temperature, residence time, and rotational speed. In this work, the authors of this paper presented the successful synthesis of NCM811 cathode materials and their electrochemical characterization in LIB full-cells. They demonstrated promising performance that can be further improved by systematic adjustment of synthesis conditions for an optimum particle design.

Acknowledgments
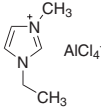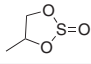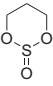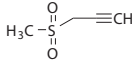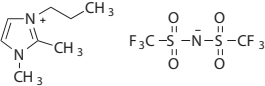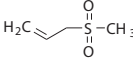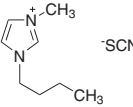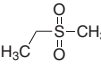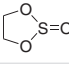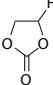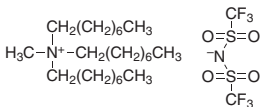
References
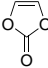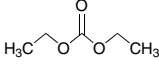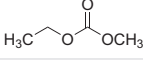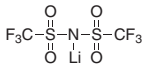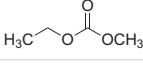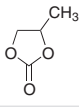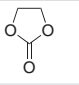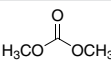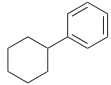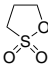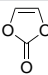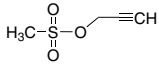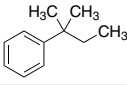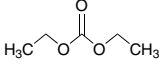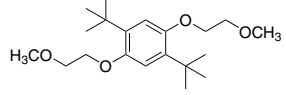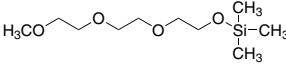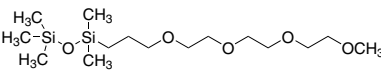
(1) Liang, Y.; Zhao, C.-Z.; Yuan, H.; Chen, Y.; Zhang, W.; Huang, J.-Q.; Yu, D.; Liu, Y.; Titirici, M.-M.; Chueh, Y.-L.; Yu, H.; Zhang, Q. *InfoMat* **2019**, *1*, 6.
(2) Schmuch, R.; Wagner, R.; Hörpel, G.; Placke, T.; Winter, M. *Nat. Energy* **2018**, *3* (4), 267.
(3) Zeng, X.; Li, M.; Abd El-Hady, D.; Alshitari, W.; Al-Bogami, A. S.; Lu, J.; Amine, K. *Adv. Energy Mater.* **2019**, *9*, 1900161.
(4) Andre, D.; Kim, S.-J.; Lamp, P.; Lux, S. F.; Maglia, F.; Paschos, O.; Stiaszny, B. *J. Mater. Chem. A* **2015**, *3*, 6709.
(5) Li, W.; Erickson, E. M.; Manthiram, A. *Nat. Energy* **2020**, *5*, 26.
(6) Myung, S.-T.; Maglia, F.; Park, K.-J.; Yoon, C. S.; Lamp, P.; Kim, S.-J.; Sun, Y.-K. *ACS Energy Lett.* **2017**, *2* (1), 196.
(7) Schmiegel, J.-P.; Qi, X.; Klein, S.; Winkler, V.; Evertz, M.; Nölle, R.; Henschel, J.; Reiter, J.; Terborg, L.; Fan, Q.; Liang, C.; Nowak, S.; Winter, M.; Placke, T. J. *Electrochem. Soc.* **2019**, *166* (13), A2910.
(8) Li, H.; Cormier, M.; Zhang, N.; Inglis, J.; Li, J.; Dahn, J. R. *J. Electrochem. Soc.* **2019**, *166* (4), A429.
(9) Aishova, A.; Park, G.-T.; Yoon, C. S.; Sun, Y.-K. *Adv. Energy Mat.* **2019**, 1903179.
(10) Betz, J.; Brinkmann, J.-P.; Nölle, R.; Lürenbaum, C.; Kolek, M.; Stan, M. C.; Winter, M.; Placke, T. *Adv. Energy Mater.* **2019**, *9* (21), 1900574.
(11) Börner, M.; Horsthemke, F.; Kollmer, F.; Haseloff, S.; Friesen, A.; Niehoff, P.; Nowak, S.; Winter, M.; Schappacher, F. M. *J. Power Sources* **2016**, *335*, 45.
(12) Wang, D.; Belharouak, I.; Koenig, G. M.; Zhou, G.; Amine, K. *J. Mater. Chem.* **2011**, *21* (25), 9290.
(13) Krumdick, G.; Shin, Y.; Kahvecioglu Feridun, O. Process Development and Scale up of Advanced Active Battery Materials. Talk at the *2015 Annual Merit Review and Peer Evaluation meeting (AMR)*, June 10, 2015.
(14) Wang, D.; Belharouak, I.; Ortega, L. H.; Zhang, X.; Xu, R.; Zhou, D.; Zhou, G.; Amine, K. *J. Power Sources* **2015**, *274*, 451.
(15) Kim, J.-M.; Chang, S.-M.; Chang, J. H.; Kim, W.-S. *Colloid. Surface. A* **2011**, *384* (1), 31.
(16) Choi, M.; Kim, H.-S.; Kim, J.-S.; Park, S.-J.; Lee, Y. M.; Jin, B.-S. *Mater. Res. Bull.* **2014**, *58*, 223.
(17) Kim, J.-E.; Kim, W.-S. *Cryst. Growth Des.* **2017**, *17* (7), 3677.
(18) Mayra, Q.-P.; Kim, W.-S. *Cryst. Growth Des.* **2015**, *15* (4), 1726.
(19) Thai, D. K.; Mayra, Q.-P.; Kim, W.-S. *Powder Technol.* **2015**, *274*, 5.
(20) Ho Shin, Y.; Kahvecioglu Feridun, O.; Krumdick, G. *Material Matters* **2014**, *9* (4), 131.
(21) Kwade, A.; Haselrieder, W.; Leithoff, R.; Modlinger, A.; Dietrich, F.; Droeder, K. *Nat. Energy* **2018**, *3* (4), 290.
(22) Ochoa, J.-C.; Coufort, C.; Escudié, R.; Liné, A.; Paul, E. *Chem. Eng. Sci.* **2007**, *62* (14), 3672.
(23) Laminar, http://www.laminarm.co.kr (Accessed: February 5th, 2020).

Precursor Materials

Name	Composition	Form	Purity	Cat. No.
Nickel(II) sulfate hexahydrate	$NiSO_4 \cdot 6H_2O$	crystals	≥98%	**227676-100G** **227676-500G** **227676-1KG** **227676-2.5KG**
Cobalt(II) sulfate heptahydrate	$CoSO_4 \cdot 7H_2O$	powder	≥99%	**C6768-100G** **C6768-250G** **C6768-1KG** **C6768-2.5KG**
Manganese(II) sulfate monohydrate	$MnSO_4 \cdot H_2O$	powder	≥99%	**M7634-100G** **M7634-500G** **M7634-1KG**
Sodium Hydroxide, Pellets - CAS 1310-73-2 - Calbiochem	NaOH	pellets (crystalline)	≥95%, titration	**567530-250GM** **567530-500GM**
Lithium-7Li2 carbonate	$^7Li_2CO_3$	-	99% (CP)	**601470-5G** **601470-10G**
Ammonium hydroxide solution	NH_4OH	NH_3 28% in H_2O	≥99.99% trace metals basis	**338818-5ML** **338818-100ML** **338818-1L**
Lithium hydroxide monohydrate	$LiOH \cdot H_2O$	powder or granules	≥98.0%	**402974-25G** **402974-500G** **402974-2KG**

Solvents and Additives

Name	Structure	Purity	Cat. No.
1-Ethyl-3-methylimidazolium tetrachloroaluminate, for energy applications		99.9% trace metals basis	**724424-5G**
1,2-Propyleneglycol sulfite		≥98%	**774456-10G**
1,3-Propylene sulfite		99%	**774243-25G**
3-(Methylsulfonyl)-1-propyne		95%	**718319-5G**
1,2-Dimethyl-3-propylimidazolium bis(trifluoromethylsulfonyl)imide, for energy applications		99.9% trace metals basis	**724416-1G**
Allyl methyl sulfone		96%	**718203-5G**
1-Butyl-3-methylimidazolium thiocyanate, for energy applications		≥95%	**724408-5G**
Ethyl methyl sulfone, for energy applications		97%	**709980-5G**
Ethylene sulfite		≥99.0%	**774251-25G**
Fluoroethylene carbonate		99%	**757349-25G**
Methyl-trioctylammonium bis(trifluoromethylsulfonyl)imide, for energy applications		99.9% trace metals basis	**724432-1G**

Name	Structure	Purity	Cat. No.
Vinylene carbonate		99%	**757144-25G**
Diethyl carbonate, anhydrous		≥99%	**517135-100ML** **517135-1L**
Acetonitrile, electronic grade	CH_3CN	99.999% trace metals basis	**733466-1L** **733466-4L**
Ethyl methyl carbonate		99%	**754935-50ML**
Bis(trifluoromethane)sulfonimide		-	**449504-10G** **449504-50G**
Ethyl methyl carbonate, Acid content: <10 ppm H_2O <10 ppm acid <10 ppm		99.9%	**809934-25G** **809934-500G**
Propylene carbonate, H_2O <10 ppm acid <10 ppm		≥99%	**809969-25G** **809969-500G**
Ethylene carbonate, H_2O <10 ppm acid <10 ppm		≥99%	**809950-25G** **809950-500G**
Dimethyl carbonate, H_2O <10 ppm acid <10 ppm		≥99.9%	**809942-25G** **809942-500G**
Phenylcyclohexane, H_2O <100 ppm acid < 200 ppm		≥99%	**810002-25G** **810002-500G**
1,3-Propanesultone, Acid content: <10 ppm H_2O <100 ppm acid <200 ppm		≥99%	**809985-25G** **809985-500G**
Vinylene carbonate, H_2O <100 ppm Moisture: <10 ppm Acid content: <10 ppm acid <200 ppm		99.5%	**809977-25G** **809977-500G**
2-Propynyl methanesulfonate, Acid content: <200 ppm H_2O <100 ppm Moisture: <100 ppm acid <200 ppm		≥99.5%	**809993-25G** **809993-500G**
tert-Amylbenzene		≥99%	**900001-1EA** **900001-25G** **900001-500G**
Diethyl carbonate, H_2O <10 ppm acid <10 ppm		≥99%	**900018-25G** **900018-500G**
Adiponitrile, H_2O <100 ppm acid <200 ppm		>99%	**900020-25G** **900020-500G**
1,4-Di-*tert*-butyl-2,5-bis (2-methoxyethoxy) benzene, anhydrous		99.5%	**900797-5G** **900797-25G**
2,2-Dimethyl-3,6,9,12-tetraoxa-2-silatridecane		≥98%	**900871-5G** **900871-25G**
2,2,4,4-Tetramethyl-3,8,11,14,17-pentaoxa-2,4-disilaoctadecane		99%	**900763-5G** **900763-25G**

Advancements in Quantum Dot Solar Cells: Synthesis and Applications
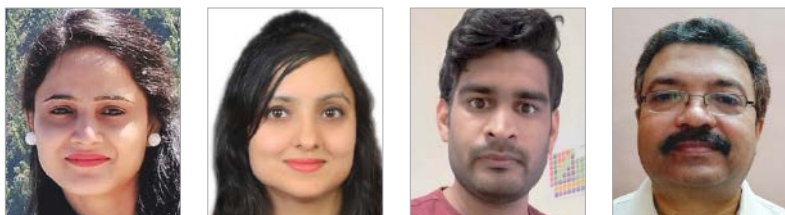
Pooja Semalti,[1,2] **Swati Bishnoi,**[1,2] **Parth Vashishtha,**[3]* **Shailesh Narain Sharma**[1,2]*

[1] Academy of Scientific and Innovative Research (AcSIR), Council of Scientific & Industrial Research (CSIR) — Human Resource Development Centre, (CSIR-HRDC) Campus, Ghaziabad, Uttar Pradesh 201002, India
[2] CSIR-National Physical Laboratory (NPL), Dr. K.S. Krishnan Road, New Delhi 110012, India
[3] School of Materials Science and Engineering, Nanyang Technological University (NTU), 50 Nanyang Avenue, Singapore 639798, Republic of Singapore
* Email: pvashishtha@ntu.edu.sg, shailesh@nplindia.org

Introduction

Nanomaterials (NMs) are a class of materials attaining remarkable attention in several research areas due to their tunable physical, chemical, and biological properties. NMs exhibit superior electronic, optical, and chemical characteristics in comparison to their bulk counterparts due to their enhanced surface to volume ratio and the quantum confinement effect. Among NMs, quantum-dots (QDs) are one of the most fascinating, as they show improved optoelectronic properties by the "quantum confinement effect". QDs have tremendous applications in photovoltaic cells, transistors, LEDs, lasers, photodetectors, quantum computing, and biological imaging.[1,2]

Quantum dots are based on the theory of quantum confinement, which comes into play when the diameter of the nanoparticle is of the order of the electron's wavelength. Whenever the particle's dimension reaches this critical size, the electronic and optical properties of that nanoparticle substantially deviates from its bulk counterpart. In the quantum confinement effect, the particle behaves as a free particle when the confinement dimensions are large as compared to the wavelength of the particle. At this state, the bandgap remains at its original energy due to a continuous energy state. However, when the confining dimension decreases and a specific size limit has been achieved by the particle, the continuous energy state spectrum changes to a discrete energy state spectrum. Resulting in the bandgap dependency on the size of nanoparticle becomes more prominent, as shown in **Figure 1**. The spectrum of colors in quantum dots relies on this energy, as the size of the quantum dot increases, this results in a red-shift (lower energy), and as

the size decreases, there is a blue-shift (higher energy) as shown in **Figure 2**. In short, quantum confinement is the reason for the increase in the energy difference between bandgap and energy states. In **Figure 1**, the band structure of bulk semiconductors absorbs light (photons) having > energy bandgap (E_g). In the case of semiconductor cells, photo-generated carriers thermalize to band edges (within about 10^{-13} s) as excess energy is lost as heat, reducing output. This limitation reduces current, while the thermalization reduces the voltage. As a result, semiconductor cells suffer a trade-off between voltage and current, which can be in part alleviated by using multiple junction implementations.
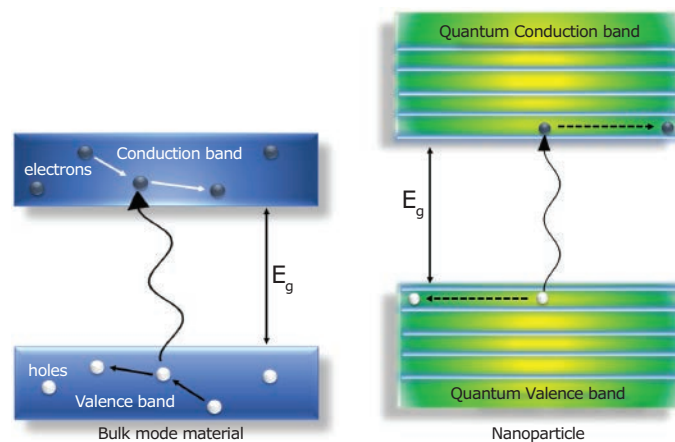
Figure 1. Energy-Band diagram of semiconductor bulk and nanomaterials
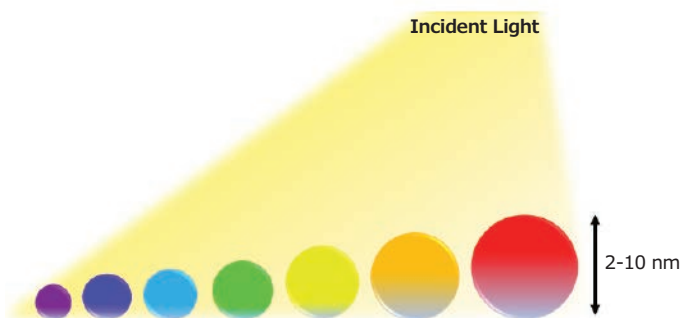
Figure 2. Representative quantum-dots of a particular wavelength

However, in the case of quantum dots, the QD absorption (bandgap) can be tuned to match incident light and extract carriers without loss of voltage due to thermalization. Thus, solar cells that incorporate QDs may lead to more efficient light-harvesting and energy conversion.

QD based photovoltaic cells have also emerged tremendously in recent years as QDs have the potential of enhancing the power conversion efficiency (PCE) of the photovoltaic devices (PV) beyond the traditional Shockley and Queisser limit, which is 32% in case of Si-based PV cells.[3,4] Semiconductor QDs used in PV devices offer serval advantages as light harvesters. First, their size-based quantum confinement enables us to tune their optical response. Furthermore, these QDs offer ways to make use of the hot electrons or to generate multiple charge carriers from a single photon.[5] However, limitations of the QDs based PV cells are the potential for defects, which leads to undesirable recombination and hence, limits the PCE of the resultant device.

Various strategies have been suggested by researchers to overcome these issues. Our review provides a brief overview of efficient QDs, synthesis, strategies for designing QDs based PV cells, shortcomings, and suggestions to overcome the drawbacks that limit efficiency. This review covers the significant aspects of QD solar cells (QDSCs), which are essential to understand to improve this field and its commercialization further.

Nanomaterial Synthesis

Nanomaterials can be synthesized using various techniques, including both physical and chemical methods; both are described below. The physical methods include techniques such as gas condensation, chemical vapor deposition, atomic layer deposition, and pulsed laser depositions. The chemical methods, such as heat-up technique, hot-injection technique, re-precipitation method, and hydrothermal synthesis, are also discussed. Each of these methods has advantages and disadvantages for synthesis.

Gas Condensation

In this technique, the vaporization of a metallic or inorganic precursor material occurs using thermal evaporation in 1–50 m bar atmospheric pressure. The formation of fine particles with a dimension of 100nm by the collision of evaporated atoms with residual gas molecules results from 'gas evaporation'.

Vacuum Deposition Process

Another commonly used physical technique in which the deposition of compounds/alloys occurs in a vacuum after vaporization. The process requires an ambient pressure <0.1m bar via gas to provide collision and cooling for nucleation, resulting in particles or clusters in the range of 1–100 nm.

Chemical Vapor Deposition (CVD) and Chemical Vapor Condensation (CVC)

The CVD process involves a chemical reaction between volatile precursors and the surface of the materials to be coated. In CVD, a precursor gas(es) a flowed into a chamber containing one or more heated objects required to coat. The chemical reactions occur near hot surfaces, resulting in the deposition of a thin film on the surface. CVD has relatively high deposition rates but requires volatile precursors and elevated temperatures, limiting its applicability for wide range of materials.

Pulsed Laser Deposition (PLD)

Pulsed laser deposition uses a high-power pulsed laser beam, which is focused on a target of the material that is to be deposited. The process happens in a vacuum chamber, where the vaporized target material (in a plasma plume) is deposited as a thin film on a substrate.

Mechanical Attrition or Ball Milling

Another physical technique that produces nanostructures by the structural-decomposition of coarser grain-structures resulting from plastic deformation is mechanical attrition or ball milling.

Chemical Synthesis of Nanocrystals

Heat-Up Technique

The heat-up technique is a non-injection method in which the precursor is heated steadily in the presence of ligands. To perform this technique, mix the required precursors at room temperature, and then increase the heat to the suitable growth temperature. Most of the heat-up synthesis techniques deliver polydisperse particles due to the random nucleation that occurs over different time scales. Copper Indium Sulphide (CIS) QDs are generally synthesized using this method for applications in PV devices.

Hot-Injection Technique

In this technique, a room temperature precursor solution is injected into a hot reaction medium in the presence of suitable surfactant molecules. The precursor solution initiates monomer formation, and due to their supersaturation, causes nuclei formation. After the injection of room temperature precursor, the reaction temperature reduces and the precursor solution is quickly reacts with remaining precursor causing the prevention of further nucleation. Overall, the growth of nanocrystals occur at lower temperature than nucleation's temperature. This temperature decrease creates an energy barrier for nucleation, resulting in uniform-sized particles of the desired material. The synthesis of highly luminescent CdSe nanocrystals using this technique occurs by injection of a room temperature solution of precursor molecules into hot (300 °C) trioctylphosphine oxide (TOPO).

Ligand Assisted Reprecipitation Method

Ligand-assisted re-precipitation (LARP) technique is an efficient method for the synthesis of organometal halide perovskite nanocrystals (PNCs). Zhang et al. initially introduced the LARP approach for the synthesis of MAPbX$_3$ NCs.[6] In this method, the preparation of an initial solution occurs by adding the lead halide and organic halide salt precursors into a polar solvent such as dimethylformamide dimethylformamide (DMF) or Dimethyl sulfoxide (DMSO) in the presence of ligands such as octylamine and oleic acid. Then, the dropwise addition of this solution into a non-polar medium (such as toluene). **Figure 3** shows the schematic diagram for the synthesis. The miscibility gap between both solvents initiates the recrystallization of lead halide perovskite NCs. After the formation of nanocrystals, the purification needs to be carried out at high RPM (2 times) using a centrifuge machine. LARP method is viable for industrialization and scalability purpose. While LARP method offers an economical route to prepare high quality nanocrystals; it still hamper the precise control of reaction conditions in contrast to hot-injection route. Overall, less control on shape and size of nanocrystals is an issue in LARP method.

Metal halide perovskite precursor salts in polar solvent (DMF)

Non-Polar Solvent (toluene) with amine ligands

Figure 3. Schematic diagram showing the ligand-assisted re-precipitation (LARP) method. Reprinted with permission from reference 6, copyright 2019 American Chemical Society.

Hydrothermal Synthesis

This technique finds use in the synthesis of nanocrystals of different chemical compounds in a closed system such as an autoclave, that can withstand high temperature and pressure over time. All the physical and chemical processes in the autoclave occur at temperatures above 100 °C and pressures above 1 atm. The hydrothermal technique allows for the synthesis of zeolites, QDs of various oxides and carbon, and various luminescent perovskites.

Classification of Semiconductor QDs Based Solar Cells

CdSe (Cadmium Selenide)

CdSe is a well-known semiconducting material consisting of a direct band of 1.74 eV at room temperature, belongs to the II-VI group of semiconductors, and highly favors wide range optical absorption in the visible range. Most of the earlier research extensively focused on the synthesis of CdSe nanocrystal, especially with the synthesis of QDs due to ease of bandgap tunability with controlled size growth.[7,8] The outstanding fluorescence of CdSe materials make them ideal for use in various light-harvesting applications, especially photovoltaics. S. N. Sharma et al.[9] demonstrated a photoinduced charge transfer between CdSe QDs and p-phenylenediamine (ppd). They found that the formation of ppd cation radicals and other charged species at the surface extends the bleaching recovery over several microseconds. To facilitate carrier injection and light-absorption in QD solar cells, the energy levels of quantum dots should match appropriately, as seen in the cases of CdS/CuInS$_2$, CdSe/CdTe and CdS/CdSe[10,11] core/shell QD structures. The CdS/CdSe core/shell structure is one of the most widely explored QD structure owing to its easy synthesis, high stability with an efficiency (PCE) ~ 5%. Currently, the highest performing QD solar cells exhibit a PCE of only 6–8% due to the severe charge-recombination and low photoanode area coverage. To encounter this situation, mesoporous photoanodes required to employ to enhance electron transport and large area acquisition. The best performing QD solar cells contain TiO$_2$ as a mesoporous photoanode because of its low-cost and excellent chemical stability. Linkers, such as MPA-mercaptopropionic acid, have also been used for TiO$_2$ film coating, followed by exposures to QDs for QDSC assembly.[12]

InP (Indium Phosphide)

InP (group III–V) is one of the most promising materials for photovoltaic applications, with an appropriate band gap (1.35 eV), higher mobilities, and a high absorption coefficient. InP shares the lowest intrinsic toxicity as compared to Cadmium based cells. The use of different capping ligands help to overcome the size effect and bandgap tunability. Highly luminescent InP QDs with a bluish-green emission (λ~490 nm) has been reported by synthesis using the hot injection technique, with trioctyl phosphine (TOP) as the source of P instead of the conventional but toxic and expensive tristrimethylsilyylphosphine (P(SiMe$_3$)$_3$) without resorting to any post-synthesis etching to tune the emission to the blue region.[13] InP QDs are attractive due to their higher photostability and their strong covalent bond. Due to these properties, InP is one of the favorite materials for use in QDSCs. Although the strong covalent bond may cause complications for monodisperse nanoparticle synthesis, which in turn produces defects and cause a lower luminescence efficiency, to overcome the stability situation, modification to time, temperature, and choice of ligands is crucial. Other disadvantages of InP include low photocurrent due to the electron loss at the QD-electrolyte

interface, which requires QD loading with enough surface area utilization in a broad range of visible spectra. Furthermore, the size of the QD can be tuned to increase the light-harvesting range. While doping can be useful for tuning the QD to the visible spectra.[13,14]

PbS (Lead Sulphide)

PbS QDs are a promising nanostructured material for photovoltaic applications. PbS is known as a photo absorber in the visible and near infra-red regions, due to its bandgap tunability and solution processability and is also considered a low-cost solution-processed photovoltaic material. Rapid advancement in quantum solar-cells by architecting and surface modification led to a power conversion efficiency of 11.3% with outstanding stability. However, the ligand exchange process renders the manufacturing of the QD device. The choice of capping ligand (oleic acid, MPA, thiols, etc.) plays a crucial role in the stability of QDs. A typically used capping ligand, oleic acid, both stabilizes and helps to passivate the surface, making it insulated from surrounding QDs. It also allows interdot distance adjustment, which defines the coupling strength between the inter-related QDs.[15] An enhanced efficiency of 8.45% was reported for conventionally structured PbS QD solar cells, in which a modified anode buffer layer comprising of a unique conjugated polymer PDTPBT was used. This anode modification improved the device performance due to increased hole extraction to the anode and reduced interfacial carrier recombination which enhanced Voc significantly.[16]

PbSe (Lead Selenide)

PbSe is one of the reliable colloidal QDs for the next-generation photovoltaics. Previously, PbS QDs were the primary research focus due to their stability under extreme conditions. There is much interest in expanding the work to PbSe QDs, which shows increased photocurrent due to multiple generations of excitons. The synthesis of a range of sizes is required to overcome the stability issues of using PbSe ambient conditions.[17] Air stable PbSe QDs were firstly synthesized by the cation exchange method, followed by the solution-phase ligand-exchange approach. Then the absorber layers were prepared using the single-step spin coating method, which in turn shows an excellent efficiency of 10.68%, which was nearly 16% higher than earlier recorded data. The stability of that prepared cell remains stable up to 40 days with eight hours of continuous illumination. The performance of PbSe QD solar cells was improved further by introducing SnO_2 based buffer layer at the interface ETL/PbSe, and this leads to better extraction of charge carriers. Band alignment between the PbSe QD absorber layer and the TiO_2 buffer layer could be attributed to the performance enhancement of the cell.[13,18] **Figure 4** shows the schematic for the fundamental QD base solar-cell structure.

CIS (Copper-Indium/Selenide)

Copper-indium-selenide ($CuInSe_2$) is a p-type semiconductor that has drawn tremendous attraction in the field of photovoltaic applications due to its wide bandgap (1.04 eV) and significant absorption coefficient with high stability. It is considered an
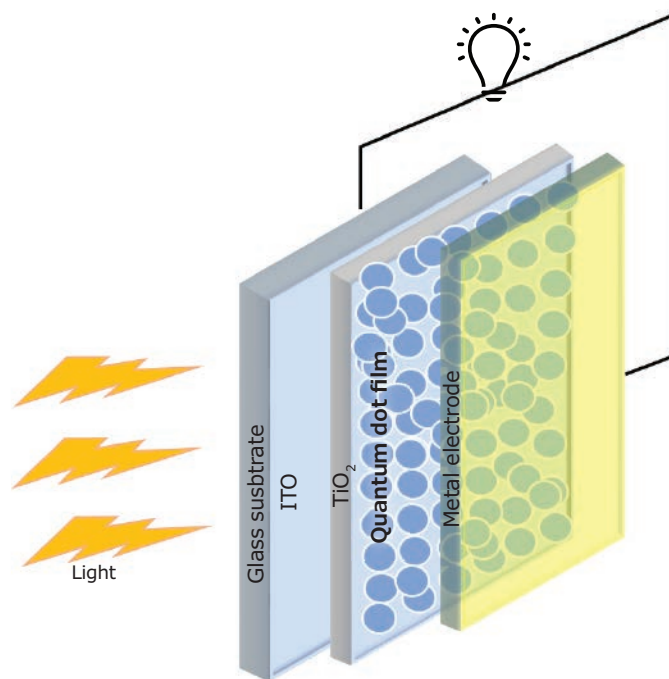
Figure 4. Schematic diagram of a quantum-dot solar-cell.

alternative to the cadmium/lead-free toxic elements. In 1976 a CIS solar cell was fabricated, with an efficiency of ~ 5%, using the evaporation technique.[19] The parameters of the cell remain stable over a long time, provided the temperature does not exceed 90 °C. Unfortunately, even after many precautions, such as placing the assembly in a glass encapsulation, their life does not exceed more than ten years. Moreover, indium resource limitations are a significant concern.[20] The cell efficiency typically depends on the crystalline nature/structure of the material formed and the share of the Indium and Copper element, In the case of CIS, the hole concentration decreases as the concentration of Copper decreases. The efficiency of CIS increased to 7% when introducing CdS as the absorber layer. Both CIS and CdS show low resistivities when deposited by vapor deposition. Further technological improvement in junctions enables the maximum photon absorption and drags the efficiency to 10%.[19] **Figure 5** shows the Schematic diagram representing CIS based Solar-cell.

CIGS (Copper-Indium/Gallium/Selenide)

Several different research technologies emerged, leading to the incorporation of gallium in the CIS cell, also known as CIGS. Following the addition of Gallium (Ga), sodium (Na) has also been incorporated into the absorber layer of CIGS cell assembly with a thin layer of CdS as a buffer layer, which has significantly enhanced the cell efficiency to 22.6%.[20-22] CIGS formation follows two-steps, the optimized CIG precursors are deposited onto a substrate; this could be done by sputtering, vapor deposition, or and electrodeposition. In most of CIG (S, Se) deposition, Ink deposition is trending due to the low material utilization, with less waste and ease of preparation. **Figure 5** shows the Schematic diagram representing CIS based Solar-cell. Sharma et
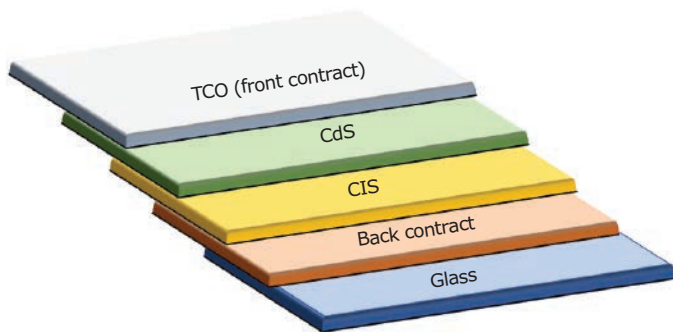
Figure 5. Schematic diagram representing a CIS based solar cell.

al. reported an aqueous-free based rapid synthesis (~ 45 mins.) of organically-capped Se-rich CIGSe by the colloidal route.[23] They reported a process of purification which elevated the charge-transport between CIGSe nanocrystals for the realization of an efficient photovoltaic device without resorting to soda-lime-glass (SLG), harsh chemical treatments, or post-deposition thermal selenization.

However, sputtering has proven to be the most efficient method with respect to the cell efficiency. Ga is required to incorporate into Cu targets since Ga has a very low melting point. Stacking sequences of precursor layers can profoundly influence the elemental distribution through the depth of the final film. Most of the time, some Se has already incorporated by precursor layers, which are, in turn, annealed and selenized. The substrate preparation in CIGS solar cells is the most crucial and tedious process, which plays a vital role in the development of the whole device. Molybdenum deposition onto a flexible/rigid substrate defines the condition of selenization. The annealing temperature challenges the ability to create a flexible, CIGS based device. Flexible substrates cannot withstand this high temperature of 500 °C, which is a mandatory step for absorber layer crystallization in a CIGS cell. The efficiency recorded using a flexible substrate is ~20%. In CIGS structure, the role of n-semiconductor is fulfilled by ZnO as the buffer layer and CdS as the window layer; both can be replaced by each other. A schematic of the CIGS solar cell has a structure of substrate/Mo/CIGS/CdS/ZnO/metal grid (**Figure 6**). Here light enters via a Transparent conductive oxide (TCO) and a back-contact deposited on the substrate.[24]

Perovskites

Perovskites are a class of minerals with a crystalline cubic/diamond-like structure. A conventional perovskite is a calcium titanium oxide ($CaTiO_3$) mineral, first found in the Ural Mountains of Russia. The metal halide perovskite, which has a similar structure to oxide perovskites, are potential candidates for solar-cell applications. A halide perovskite has an ABX_3 crystal structure (**Figure 7**), where A is a monovalent cation, such as Cs^+, MA^+, FA^+, B is a divalent cation such as Pb^{2+} or Sn^{2+}, and X is an anion such as Cl^-, Br^-, and I^-.[25]
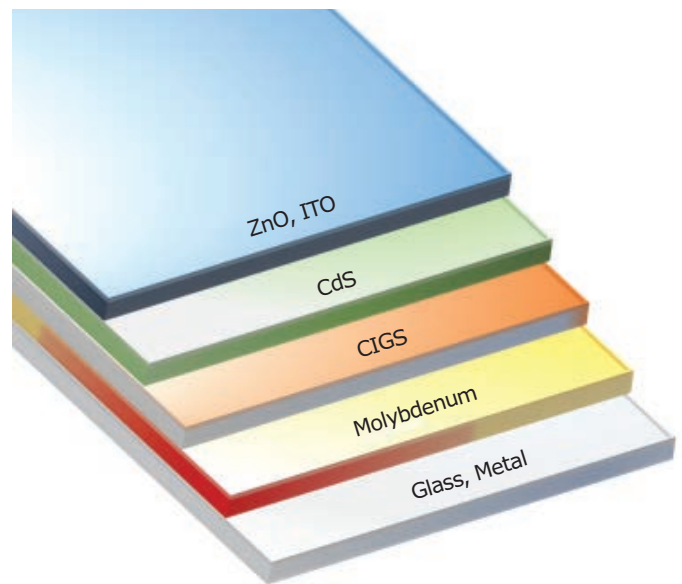
Figure 6. Schematic representing a CIGS solar-cell structure.
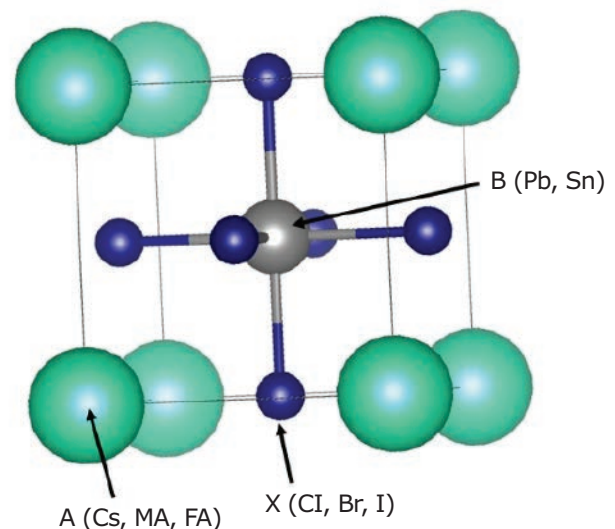
Figure 7. A Perovskite cubic crystal structure. Reprinted with permission from reference 25, copyright 2018 Victoria University of Wellington, New Zealand.

Perovskites offer several advantages in the solar cell regime. Perovskites offer composition with a tunable bandgap (1.5–2.3eV), which is the most favorable condition for maximum sunlight absorption and hence the maximum conversion of electricity.[26-28] They can be synthesized by solution processing techniques, which makes the fabrication process cost-effective when compared to conventional solar cell technologies.[29,30] Perovskites can also be used as an electron/hole transport layer to enhance charge transport. It has high charge mobility, high excitation coefficient, long carrier lifetime, carrier diffusion rate, and high absorption coefficient.[31] Furthermore, the formation of perovskite thin films requires very little material. No rare earth elements are required. Perovskites are highly tolerant of defects, which creates a large manufacturing yield.[25] The module has the

lowest environmental effect, depending upon the manufacturing method used. They can be easily deposited onto a flexible substrate, opening a new area for further research.

The disadvantages of perovskites are their environmental induced (moisture, oxygen, and light) stability issues. However, due to the rapid advancements in cell efficiency, researchers have overcome many of these limitations by providing a standardized packaging assembly. Other stability issues like mechanical durability, thermal influence, applied voltage heating, and current-voltage behavior require further detailed study.

Most efficient metal halide perovskite is composed of lead (Pb) based material, such as, $FAPbI_3$, $MAPbI_3$, and $CsPbI_3$. Figure 8 shows the schematic of a perovskite solar cell. Currently, researchers have achieved very high efficiencies (>25%) with perovskite-based solar cells.[32] The National Center of Photovoltaics (NCPV) has shown that when carriers are excited with high energy, the cooling rate in perovskite materials slows down during the cooling process. The cooling occurs more slowly when using $MAPbI_3$ as compared to other traditional and expensive structures, making this material an excellent candidate for next-generation hot carrier solar cells with high efficiency. Since excitons do not remain stable at room temperature, the coulomb interaction between carriers (electrons and holes) dramatically affects the optical absorption in these materials, and the presence of excitons impacts on recombination dynamics.

Researchers found that even on the non-passivated surfaces, the surface recombination is significantly slower than that of recombination in other non-passivated semiconductors.[33] The toxicity of lead in perovskites is a severe threat to the environment; therefore, lead-free perovskite structures have
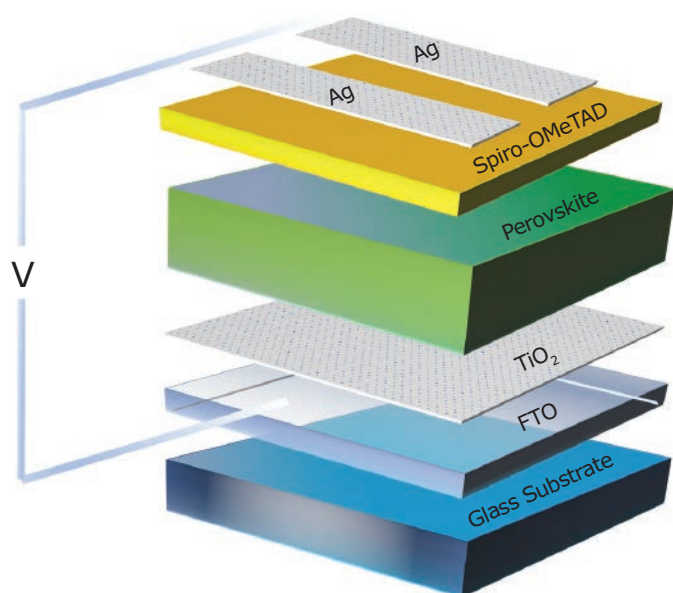
become a driving force in research. The Sn-based perovskites systems studied so far, exhibit poor film morphology and uncontrolled crystallization, which limit the actual potential of perovskites. Although many additives such as SnF_2, $SnCl_2$, etc. overcome some of these effects, unfortunately, the stability and efficiency have not been up to current standards of lead-based perovskites. More research is required to address this problem using different permutations and combinations of materials.

Challenges Ahead and Future Scope

In the past few years, QD based PV devices, especially perovskite solar cells, have improved significantly in terms of efficiency, but their stability is still a matter of concern. One possible solution in this direction to improve the stability of perovskite-based PV devices is by minimizing the perovskite dimensionality. The stability of layered 2D films and nanocrystal QDs based PV cells are still better than the perovskite 3D film-based devices. Also, the QDs of perovskites have better phase stability and composition tunability in comparison to thin-film perovskites. Despite all this, the highest reported efficiency of QDs based device is 13.4%, still much lesser than 25.2% reported for a thin-film perovskite device.[35,36] To address the issue of low efficiency, Hao et al., synthesized multi-cation perovskites using the oleic acid (OA) ligand-assisted cation exchange method and they got an enhanced efficiency of more than 16%.[31] Surface trap defects also limits the efficiency of QDs based PV cells. To overcome this issue, core-shell architecture based QDs were designed in which a shell of wider bandgap material (CdS) was over-coated around the core (CdSeTe). This architecture minimizes the surface defects and boosts the PCE of the resultant device.[32] Similarly, to reduce the charge recombination at the interface of photoanode/electrolyte in QDPV cells, the concept of the passivation layer was introduced. The passive layer deposition minimizes the charge recombination and restricts the movement of electron in the electrolyte, which is one of the reasons for the limited efficiency of quantum dot solar cells (QDSCs).[21,37] In spite the previously mentioned measures to improve the stability and efficiency of QDSCs, there are still two significant challenges in the path of their commercialization. The first is the high processing cost of QD materials, and the other is the need for efficient deposition methods for QDSCs fabrication. Hence, efforts are needed to minimize the cost of QD synthesis and device fabrication to ensure better commercialization of QDSCs. Also, the current method for QDSC fabrication relies on the spin-coating technique for the layered deposition of perovskites films, which can't be scaled up for mass production. Hence, significant research is still required in this domain to resolve the various existing drawbacks in the QDSC technology for the successful commercialization of high-efficiency stable QD PV devices. Lead-free perovskites are also emerging as an environmental-friendly substitute for lead-based perovskites, but a lot for research is still required to improve their efficiency and stability so that it can match with that of lead-based perovskites.

Figure 8. Schematic representing a perovskite solar cell prototype.

Conclusion

In this article, we reviewed the recent research in the area of quantum dot solar cells in terms of the QDs synthesis methods, their advantages and disadvantages, literature review of the recently developed QDSCs devices, their architecture, and their efficiencies and shortcomings. We have discussed in detail the working mechanism of several QDSCs, including CdSe, CIS, PbS, PbSe, InP, perovskites, etc. and their highest reported efficiencies to date. Apart from this, we have described the factors responsible for the limited efficiency and stability of the QDSCs and their possible solutions, as suggested by different research groups. The article highlights how the rapidly progressing QD based PV devices are emerging and, in the future could surpass the Si photovoltaics in terms of efficiency and stability.

Acknowledgments

References

(1) Tada, H.; Fujishima, M.; Kobayashi, H. *Chem. Soc. Rev.* **2011**, *40* (7), 4232–4243.
(2) Santra, P. K.; Kamat, P. V. *J. Am. Chem. Soc.* **2012**, *134* (5), 2508–2511.
(3) Nozik, A.J. *Physica E Low Dimens. Syst. Nanostruct.* **2002**, *14* (1–2), 115–120.
(4) Kongkanand, A.; et al. *J. Am. Chem. Soc.* **2008**, *130* (12), 4007–4015.
(5) Ross, R. T.; Nozik, A. J. *J. Appl. Phys.* **1982**, *53* (5), 3813–3818.
(6) Zhang, F., et al. *ACS Nano.* **2015**, *9* (4), 4533–4542.
(7) Mehta, A., et al. *Physics of Semiconductor Devices*; Springer International: Switzerland 2014; pp 315–318.
(8) Zhang, H., et al. Chem. Commun. **2012**, *48* (91), 11235–11237.
(9) Sharma, S. N.; Pillai, Z. S.; Kamat, P. V. *J Phys. Chem. B* **2003**, *107* (37), 10088–10093.
(10) Huang, K. -Y., et al. *Nano. Res. Lett.* **2019**, *14* (1), 18.
(11) Sharma, S.N., et al. *Sol. Energy Mater. Sol. Cells* **2012**, *100*, 6–15.
(12) Semalti, P.; Sharma, S. N. *J. Nanosci. Nanotechnol.* **2020**, *20* (6), 3647–3658.
(13) Singh, A., et al. *Physica E Low Dimens. Syst. Nanostruct.* **2017**, *90*, 175–182.
(14) Yang, S., et al. *J. Mater. Chem. A* **2015**, *3* (43), 21922–21929.
(15) Hu, L., et al. *Sol. Energy Mater. Sol. Cells* **2016**, *155*, 155–165.
(16) Lu, K., et al. *J. Mater. Chem. A* **2017**, *5* (45), 23960–23966.
(17) Zhang, J., et al. *Nano Lett.* **2014**, *14* (10), 6010–6015.
(18) Kumar, U., et al. *Mater. Chem. Phys.* **2009**, *113* (1), 107–114.
(19) Ramanujam, J.; Singh, U. P. *Energy Environ. Sci.* **2017**, *10* (6), 1306–1319.
(20) Chawla, P., et al. *Superlattice Microstr.* **2018**, *113*, 502–509.
(21) Kim, H.-J., et al. *Energies* **2018**, *11* (8), 1931.
(22) Chawla, P., et al. *Physics of Semiconductor Devices*; Springer International: Switzerland 2014; pp 351–354.
(23) Sharma, S. N., et al. *Energy Technol.* **2019**, *7* (10), 1900615.
(24) Ludin, N.A., et al. *Renew. Sust. Energ. Rev.* **2018**, *96*, 11–28.
(25) Vashishtha, P. Nanostructured Inorganic Metal Halide Perovskites for Optoelectronic Applications. Ph.D. Thesis, Victoria University of Wellington, New Zealand, 2018.
(26) Mehra, S., et al. *Energy Storage* **2019**, *2* (2), e120.
(27) Vashishtha, P.; Halpert, J. E. *Chem. Mater.* **2017**, *29* (14), 5965–5973.
(28) Eperon, G.E., et al. *Energy Environ. Sci.* **2014**, *7* (3), 982–988.
(29) Ma, Y., et al. *Solar RRL* **2017**, *1* (8), 1700078.
(30) Zhou, D., et al. *J. Nanomater.* **2018**. doi.org/10.1155/2018/8148072
(31) Motta, C.; El-Mellouhi, F.; Sanvito, S. *Sci. Rep.* **2015**, *5* (1), 1–8.
(32) Hossain, M.I., et al. *J. Mater. Chem. A* **2018**, *6* (8), 3625–3633.
(33) Yang, L., et al. *Adv. Funct. Mater.* **2019**, *29* (46), 1905694.
(34) Bishnoi, S., et al. *Optik* **2020**, *203*, 164015.
(35) Arinze, E. S. Engineering Tunable Colloidal Nanostructures for Light Energy Harvesting. Ph.D. Thesis, Johns Hopkins University, Baltimore, Maryland, 2018.
(36) Yoo, J. J., et al. *Energy Environ. Sci.* **2019**, *12* (7), 2192–2199.
(37) Kim, S., et al. *ACS Nano* **2013**, *7* (6), 4756–4763.

Cadmium-Based Quantum Dots

Core-Type Quantum Dots

CdTe

Name	Form	Description	Fluorescence Emission, λ_{em} (nm)	Cat. No.
CdTe core-type quantum dots	powder	COOH functionalized	510	**777986-10MG** **777986-25MG**
	powder	COOH functionalized	520	**777935-10MG** **777935-25MG**
	powder	COOH functionalized	570	**777943-10MG** **777943-25MG**
	powder	COOH functionalized	610	**777951-10MG** **777951-25MG**
	powder	COOH functionalized	770	**777994-10MG** **777994-25MG**
	powder	COOH functionalized	710	**777978-10MG** **777978-25MG**

Core-Shell Type Quantum Dots

CdS/ZnS

Name	Form	Description	Fluorescence Emission, λ_{em} (nm)	Cat. No.
CdS/ZnS core-shell type quantum dots	4 µM in PBS, dispersion	amine	400	**900290-250UL**
	4 µM in PBS, dispersion	amine	425	**900305-250UL**
	4 µM in PBS, dispersion	amine	450	**900304-250UL**
	1 mg/mL in H_2O, dispersion	carboxylic acid	400	**900298-1ML**
	1 mg/mL in H_2O, dispersion	carboxylic acid	425	**900299-1ML**

Name	Form	Description	Fluorescence Emission, λ_{em} (nm)	Cat. No.
CdS/ZnS core-shell type quantum dots	1 mg/mL in H₂O, dispersion	carboxylic acid	450	**900294-1ML**
	lyophilized powder solid	carboxylic acid	400	**900310-1MG**
	lyophilized powder solid	carboxylic acid	425	**900308-1MG**
	lyophilized powder solid	carboxylic acid	450	**900332-1MG**
	powder solid	oleic acid	400	**900280-10MG**
	powder solid	oleic acid	425	**900283-10MG**
	powder solid	oleic acid	450	**900282-10MG**
	5 mg/mL in toluene, dispersion	oleic acid	400	**900286-1ML**
	5 mg/mL in toluene, dispersion	oleic acid	425	**900333-1ML**
	5 mg/mL in toluene, dispersion	oleic acid	450	**900334-1ML**
	4 µM in H₂O, dispersion	PEG	400	**900303-250UL**
	4 µM in H₂O, dispersion	PEG	425	**900302-250UL**
	4 µM in H₂O, dispersion	PEG	450	**900301-250UL**
	4 µM in H₂O, dispersion	PDDA coated	400	**900306-250UL**
	4 µM in H₂O, dispersion	PDDA coated	425	**900307-250UL**
	4 µM in H₂O, dispersion	PDDA coated	450	**900309-250UL**

CdSe/ZnS

Name	Form	Description	Fluorescence Emission, λ_{em} (nm)	Cat. No.
CdSe/CdS core-shell type quantum rods	5 mg/mL in hexane, dispersion	carboxylic acid	530	**900511-1ML**
	5 mg/mL in hexane, dispersion	carboxylic acid	560	**900512-1ML**
	5 mg/mL in hexane, dispersion	carboxylic acid	590	**900515-1ML**
	5 mg/mL in hexane, dispersion	carboxylic acid	620	**900514-1ML**
CdSe/ZnS core-shell type quantum dots	solid	stabilized with octadecylamine ligands	520	**748021-10MG** **748021-25MG**
	solid	stabilized with octadecylamine ligands	540	**748056-10MG** **748056-25MG**
	solid	stabilized with octadecylamine ligands	560	**748080-10MG** **748080-25MG**
	solid	stabilized with octadecylamine ligands	600	**748099-10MG** **748099-25MG**
	solid	stabilized with octadecylamine ligands	580	**748129-10MG** **748129-25MG**
	solid	stabilized with octadecylamine ligands	620	**790192-10MG** **790192-25MG**
	solid	stabilized with octadecylamine ligands	630	**790206-10MG** **790206-25MG**

Alloyed Quantum Dots

Name	Form	Description	Fluorescence Emission, λ_{em} (nm)	Cat. No.
CdSeS/ZnS alloyed quantum dots	1 mg/mL in toluene	oleic acid	450	**753742-25ML**
	1 mg/mL in toluene	oleic acid	490	**753750-5ML** **753750-25ML**
	1 mg/mL in toluene	oleic acid	525	**753769-5ML**
	1 mg/mL in toluene	oleic acid	540	**753777-5ML** **753777-25ML**
	1 mg/mL in toluene	oleic acid	575	**753785-5ML** **753785-25ML**
	1 mg/mL in toluene, liquid	oleic acid	630	**753793-5ML** **753793-25ML**
	1 mg/mL in toluene	oleic acid	665	**753807-5ML** **753807-25ML**
	1 mg/mL in H₂O, liquid	COOH functionalized	490	**754226-1ML** **754226-5ML**
	1 mg/mL in H₂O, liquid	COOH functionalized	525	**753831-1ML** **753831-5ML**

Name	Form	Description	Fluorescence Emission, λ_{em} (nm)	Cat. No.
CdSeS/ZnS alloyed quantum dots	1 mg/mL in H$_2$O, liquid	COOH functionalized	540	**753866-5ML**
	1 mg/mL in H$_2$O, liquid	COOH functionalized	575	**753874-1ML** **753874-5ML**
	1 mg/mL in H$_2$O, liquid	COOH functionalized	630	**753882-5ML**
	1 mg/mL in H$_2$O, liquid	COOH functionalized	665	**753890-1ML** **753890-5ML**
CdSeS/ZnS alloyed quantum dots kit	5 X 1 mg/mL in toluene	Size: 1 ml x 5 vials, oleic acid	490-665	**753823-1KT**
	5 X 1 mg/mL in H$_2$O	COOH functionalized	490-665	**753904-1KT**

Cadmium-Based Quantum Rods

Core-Shell Type Quantum Dots

CdSe/CdS

Name	Form	Description	Fluorescence Emission, λ_{em} (nm)	Cat. No.
CdSe/CdS core-shell type quantum rods	5 mg/mL in hexane, dispersion	carboxylic acid	530	**900511-1ML**
	5 mg/mL in hexane, dispersion	carboxylic acid	560	**900512-1ML**
	5 mg/mL in hexane, dispersion	carboxylic acid	590	**900515-1ML**
	5 mg/mL in hexane, dispersion	carboxylic acid	620	**900514-1ML**

Cadmium-Free Quantum Dots

InP/ZnS

Name	Form	Description	Fluorescence Emission, λ_{em} (nm)	Cat. No.
InP/ZnS quantum dots	5 mg/mL in toluene	stabilized with oleylamine ligands	530	**776750-5ML**
	5 mg/mL in toluene	stabilized with oleylamine ligands	590	**776769-5ML**
	5 mg/mL in toluene	stabilized with oleylamine ligands	620	**776777-5ML**
	5 mg/mL in toluene	stabilized with oleylamine ligands	650	**776785-5ML**
	5 mg/mL in toluene	stabilized with oleylamine ligands	560	**776793-5ML**

PbS

Name	Form	Description	Fluorescence Emission, λ_{em} (nm)	Cat. No.
PbS core-type quantum dots	10 mg/mL in toluene	oleic acid coated	1000	**747017-10ML**
	10 mg/mL in toluene	oleic acid coated	900	**900733-5ML**
	10 mg/mL in toluene	oleic acid coated	1100	**900735-5ML**
	10 mg/mL in toluene	oleic acid coated	1300	**900737-5ML**
	10 mg/mL in toluene	oleic acid coated	1500	**900728-5ML**
	10 mg/mL in toluene	oleic acid coated	1200	**747025-10ML**
	10 mg/mL in toluene	oleic acid coated	1400	**747076-10ML**
	10 mg/mL in toluene	oleic acid coated	1600	**747084-10ML**

CsPb(Cl,Br)$_3$-Based Perovskite Quantum Dots

Name	Form	Description	Fluorescence Emission, λ_{em} (nm)	Cat. No.
Perovskite quantum dots	10 mg/mL in toluene	oleic acid and oleylamine coated	450	**900748-5ML**
	10 mg/mL in toluene	oleic acid and oleylamine coated	480	**900747-5ML**
	10 mg/mL in toluene	oleic acid and oleylamine coated	510	**900746-5ML**

Advances in Conversion-Type Li-Metal Fluoride Battery: A Mini-Review

Rajesh Pathak[1], Ke Chen[1], Yue Zhou[1]*, and Qiquan Qiao [1,2]*

[1] Department of Electrical Engineering and Computer Sciences, South Dakota State
University, Brookings, SD 57007, USA
[2] Mechanical and Aerospace Engineering, Syracuse University, Syracuse, NY 13244
* Email: Qiquan.Qiao@sdstate.edu, quqiao@syr.edu and Yue.Zhou@sdstate.edu

Introduction

Conventional lithium-ion batteries (LIBs) utilize intercalation-type cathode materials, including layered $LiCoO_2$ (LCO), spinel $LiMn_2O_4$ (LMO), olivine $LiFePO_4$ (LFP), and layered $LiNi_xMn_yCo_zO_2$ (NMC).[1–2] However, these intercalating chemistries are rapidly approaching their practical achievable capacity and are currently the most significant limitation of the energy density of most commercial batteries. LIBs are the preferred energy storage device for portable electronics, electric vehicles, and grid-level energy storage but batteries with higher specific power/energy density, longer cycle life, and lower costs are still needed.[3–6] Li metal anodes combined with conversion-type lithium cathode chemistries such as lithium-metal fluoride (Li-MF) have shown tremendous potential to fulfill such requirements, owing to their higher theoretical potentials (3.55 vs. Li/Li+ for CuF_2) and higher gravimetric and volumetric capacities (713 mAh g^{-1} and 2196 mAh cm^{-3} for FeF_3).[7] In addition to CuF_2 and FeF_3, other metal fluorides such as FeF_2, CoF_2, and NiF_2 exhibit both higher theoretical discharge potential and higher volumetric capacity enabled by more than one electron transfer per transition metal.[8] The multiple reversible redox electrochemical conversion reaction is shown in **equation 1** below.[8] Besides, both fluorine and metal elements such as Fe, Cu are naturally abundant.

$$mnLi^+ + M_nX_m + mne^- \leftrightarrow mLi_nX + nM^0 \qquad (1)$$
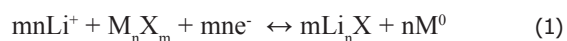
Here, "M" stands for the transition-metal ions, "X" denotes fluoride, "m" and "n" indicate the amount of lithium uptake.

Despite attractive features, multiple limitations have hindered the practical applications of MF cathodes. These barriers include low electronic conductivity, undesired side reactions with electrolytes, and the volume change during charge/discharge.[9] These features have led to poor reversibility of capacity or low coulombic efficiency, large voltage hysteresis, and quick capacity degradation upon cycling. To counter these effects, researchers have made numerous efforts to regulate the MF cathode based upon three principles: (1) structural design of cathodes, (2) stabilization of Li metal anode, and (3) selection of battery components and testing condition.

The desire to revitalize research on the Li-MF batteries has spawned successful efforts to understand and solve the challenges to provide novel concepts towards achieving high practical, specific energy, and long cycle-life. This review explores the most important concepts in designing electrochemically stable microstructures that possess wide Li-ion insertion channels and an ideal nano-morphology. Furthermore, this article evaluates the development of more suitable electrolytes by optimizing the concentration, adding additives and fillers, engineering high modulus solid electrolytes and polymer electrolytes, and *ex-situ* formation of artificial solid electrolyte/electrode interface (ASEI) in order to stabilize the Li metal anode. Additionally, this review examines the optimization and modification of the battery components and the utilization of suitable parameters and conditions during battery testing that can offer a complimentary pathway in improving the performance of the MF batteries.

Structural Design of the Cathode

Precise control over crystallization, effective prevention of particle growth and agglomeration, and establishing ideal nano-morphology of the cathode material (including wide Li-ion insertion channels) can all contribute toward improved transport and reaction kinetics of MF cathodes. However, scientists still face challenges in improving electronic conductivity, since conventional architecture based on composites or encapsulating nanosized MF in a three-dimensional (3D) carbon network still face challenges such as sluggish reaction kinetics and inhibiting the side reactions. Both binary MFs such as CoF_2 and ternary MFs such as $Ni_yFe_{1-y}F_2$ have shown great promise. Similarly, FeF_3 or FeF_2 shows high reversibility and low cost, and CuF_2 shows a high theoretical potential of 3.55 V and a high gravimetric energy density of 1874 Wh/kg.[10] However, FeF_2 has a low working potential (2.60 V) and CuF_2 is irreversible during charge/discharge cycles. The irreversibility of CuF_2 is due to the high diffusivity of Cu ions, leading to phase-separated nano metallic Cu during discharge and loss of active material due to the transport of cuprous ions during charge.

On the cathode side, substantial efforts have been made to alleviate challenges associated with active metal dissolution, electrolyte degradation, electrode volume restriction, and selective fluorine-ion percolation. Wu et al. reported a FeF_3@C composite with a 3D architecture comprised of honeycomb walls and 3D hexagonal channels. The scanning electron microscopy (STEM) and high-resolution transmission electron microscopy (HRTEM) of 3D honeycomb FeF_3@C composite are shown in **Figure 1A**. The 3D porous framework and hexagonal-like channels of carbon simultaneously enable fast electron transfer

and Li-ion transport, respectively.[9] Within the structure, the honeycomb channels range from hundreds of nanometers to a few micrometers in size. The walls of those honeycomb channels are embedded with isolated FeF_3 nanoparticles of sizes ranging from 10–50 nm.

As a result, this FeF_3@C cathode exhibited a small voltage hysteresis of ~ 0.30 V at 1C with the following properties: a mass loading of 5.3 mg cm^{-2}, 0.25–0.28 V at C-rate between C/2 and 10C with a mass loading of 1.0 mg cm^{-2}, excellent rate capabilities up to 100C, almost no capacity fading up to 200 cycles, and capacity retention of ~85% after 1000 cycles.

Wang et al. found a surprisingly small overpotential (<150 mV) by preparing solid-solution ternary MF through the substitution of Cu into the Fe lattice.[7] Here, the incorporation of Cu facilitates a collaborative redox reaction that leading to the reversible reaction $Cu^{2+}\leftrightarrow Cu^0$. The description of the reaction mechanism and phase evolution is demonstrated in **Figure 1B**. This cation substitution provided a new pathway for customizing the irreversibility issues in MF cathodes. During stages I and II the reduction of Cu and Fe occurs. During stage III, the reformation of the rutile-like Cu-Fe-F phase occurs. During higher potential (stage IV), most Cu transform back to rutile structure but some amount of Cu gets dissolved in the electrolyte or is irreversible, which implies that the final phase could have Cu-deficiency. Later on, to improve the reversibility of CuF_2, Omenya, et al. studied the presence of Fe in $Cu_{1-y}Fe_yF_2$.[10] The reversibility of $Cu_{0.5}Fe_{0.5}F_2$ is due to the presence of Fe, which shows a reversible conversion and intercalation redox reaction in the low and high voltage regions, respectively.[10]
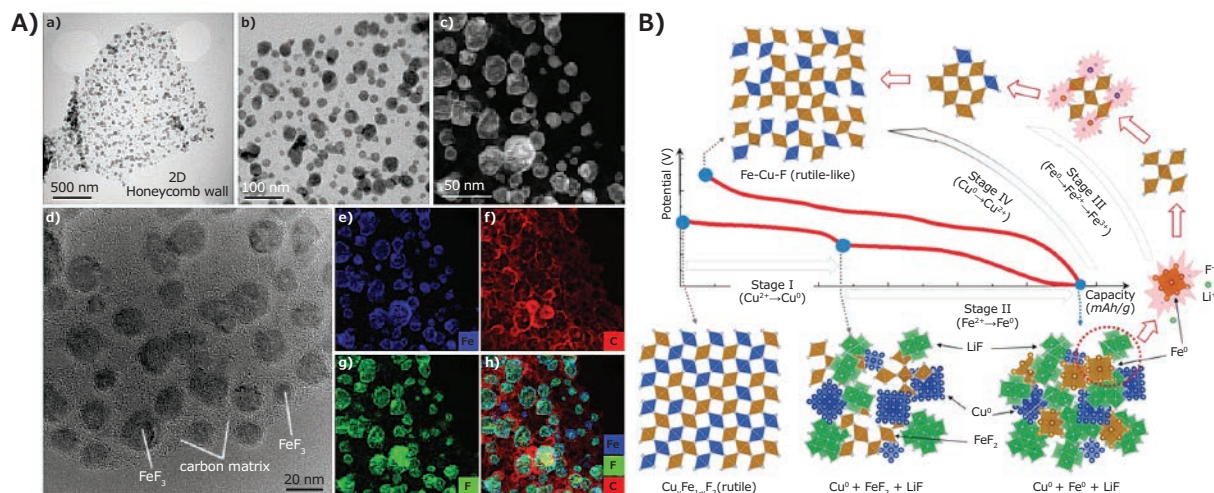
Figure 1. A) STEM and HRTEM images of 3D honeycomb carbon and FeF3 composite: (a,b) STEM, (c) HRTEM, (d) high-resolution STEM and (e-h) the corresponding elemental of iron (Fe), carbon (c), fluorine (F) and their combined mapping from (d). Reproduced with permission from reference 9, copyright 2019 Wiley-VCH. **B)** The reaction pathway of ternary $Cu_yFe_{1-y}F_2$. The reduction of Cu and Fe during initial discharge follows Stages I and II, while the oxidation of Fe and Cu follows III and IV. Reproduced with permission from reference 7, copyright 2015 Springer Nature.
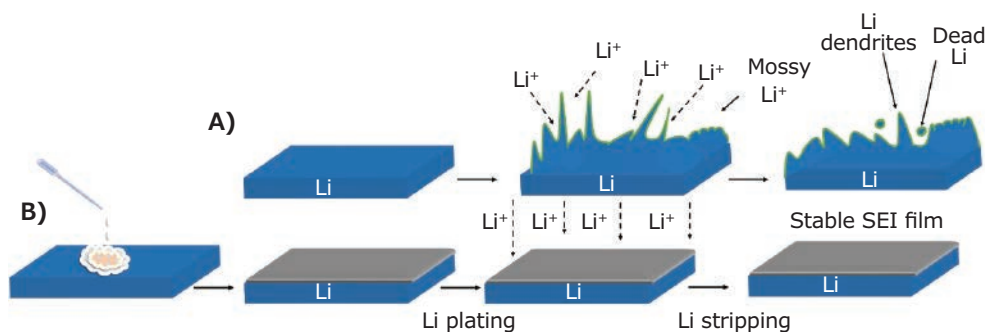
Figure 2. Schematic representation of Li plating/stripping in **A**) bare Li and **B**) SnF_2 pre-treated Li. Reproduced with permission from reference 3, copyright 2020 Springer Nature.

Further, the anion's and cation's co-substitutions (doping of cobalt and oxygen) into nanorod iron fluoride can thermodynamically lower the working potential but improves the reversibility of intercalation reaction.[11] Various strategies have been proposed to prevent the dissolution of the metal ions that causes degradation of the cathode and sluggish Li-ion transport. Potential solutions include 1) deposition of a cathode protective thin film using high-quality film uniformity and excellent conformality over high-aspect-ratio; 2) a core-shell nanostructure with an inert, thin shell of LaF_3 as an ASEI with Cu as a core; and 3) FeF_2 infiltrated into carbon mesopores.[12–14] Additionally, the *in-situ* formation of cathode SEI with a suitable choice of the liquid and solid electrolyte offers another approach to stabilize the MF-cathodes. For example, Xiao et al. obtained a capacity of 570 mAh g^{-1}, outstanding cycling stability, and more than 90% capacity retention at the charge/discharge rate of C/20.[1] Scientists accomplished this feat thanks to the formation of stable SEI and prevention of the dissolution of metal ions by the use of single-crystalline, monodisperse iron (II) fluoride nanorods and ionic liquid (1M LiFSI/Pyr$_{1,3}$FSI).

Stabilization of Li Metal Anode

Scientists have made substantial efforts to deposit Li metal dense and reversible manner, including designs that include a suitable liquid or solid electrolyte, development of stable Li host materials, as well as the development of an ASEI. The choice of Li salt, a salt concentration, and composition of the solvent determines the nature of the *in-situ* formed cathode/anode SEI. The design of suitable liquid electrolytes results in improved structural stability, flexibility, and compatibility between the anode and electrolyte interface. Such electrolytic solutions contain a combination of LiFSI-DME, acyclic organic carbonate solvents, a mixture of ADN-FEC solvent, electrolyte additives, and nitriles.[13–15] To further stabilize the Li metal anode, use of a Li ion-conducting coating, solid polymer electrolyte, and a high fluorine anion conducting tysonite-type $La_{0.9}Ba_{0.1}F_{2.9}$ have been reported.[1,6,17] The development of Li host materials and nanostructured scaffolds is another approach to accommodate Li. The lightweight nanostructure with lithiophilic sites can accommodate sufficient Li and facilitate the uniform

Li deposition, leading to improved cycling performance and lower voltage hysteresis.[5,18] In addition to that, the development of ex-situ ASEI with high chemical and mechanical stability, high ionic conductivity and Young's modulus, control on their composition, and thickness can lead to dendrite free Li deposition and stable SEI.[3–4] This leads to the control of both Li and liquid electrolyte consumption and inhibits the formation of fragile and unstable, unfavorable, overly thick SEI. **Figure 2** shows the schematic illustration of the development of SEI by drop-casting SnF_2 on the Li metal electrode. With the displacement reaction, SnF_2 and Li react to form an ASEI composed of Li-Sn alloy, LiF, and electrochemically active Sn beneficial for dendrite-free Li deposition. Moreover, the stable SEI prevents the reprecipitation of the dissolved metal ion.

Selection of Battery Components and Testing Conditions

Besides the development of advanced 3D cathode structure and stabilization of Li metal anode, the cell design principle (which consists of a selection of battery components), their modifications, and testing conditions can offer a complimentary pathway in improving the performance of the MF batteries. The use of suitable carbon additives or binders and modifying the separator with lithiophilic coatings has the potential to lead to the reversibility of MF cathodes. In addition to this, the battery testing condition, such as defining the preferred charge/discharge current density and the charge/discharge voltage limit, can also reduce the dissolution of metal and/or degradation of electrolyte. The increase in the temperature during cell testing could prove beneficial to form stable SEI and suppress Li dendrite growth that leads to enhanced rate capability and capacity utilization.[19]

Conclusions and Future Outlook

Li-MF batteries may be able to satisfy the fast-growing demand for lightweight, high-capacity, and high-energy-density storage. Momentous research efforts are underway that could bring safety, low-cost, and reversibility of the capacity, leading to the development of conversion-type Li-MF batteries that allow storage of nearly two times more volumetric energy

density and nearly three times gravimetric energy density, respectively, compared to conventional electrodes. This review summarizes the efficient approaches that have addressed the prevailing electrochemical instabilities and capacity irreversibility in MF cathodes.

In addition to the major issues covered in this review, future studies are likely to continue to focus on the essential areas of materials discovery and advanced interfacial characterization. For example, the discovery of novel computational and experimental techniques can help to identify lightweight and low-cost cathode structures to further address poor electronic conductivity, volume expansion, and dissolution of the active metal. Atomic-scale characterization and modeling techniques will help us to better understand the electrode/electrolyte interfacial chemistry required. The most effective and efficient technologies must be developed for use in practical cell application formats with a high-MF cathode mass loading, lean electrolyte, and limited ratio of the areal capacity of the negative electrode (Li) to the areal capacity of MF positive electrode (N/P). Furthermore, reproducible protocols and standards for the synthesis of the cathode structure, formation of *in-situ* or *ex-situ* anode/cathode SEI, electrolyte optimization, selection of battery components, battery fabrication, and cycling metrics are crucial for the successful deployment Li-MF battery technology.

Acknowledgments

Conflict of Interest

The authors declare no competing interests.

References

(1) Xiao, A. W.; Lee, H. J.; Capone, I.; Robertson, A.; Wi, T.-U.; Fawdon, J.; Wheeler, S.; Lee, H.-W.; Grobert, N.; Pasta, M. *Nat. Mater* 2020, *19*, 644–654. DOI: 10.1038/s41563-020-0621-z
(2) Wu, F.; Yushin, G. *Energy Environ. Sci.* 2017, *10* (2), 435–459.
(3) Pathak, R.; Chen, K.; Gurung, A.; Reza, K. M.; Bahrami, B.; Pokharel, J.; Baniya, A.; He, W.; Wu, F.; Zhou, Y. *Nat. Commun.* 2020, *11* (1), 1–10.
(4) Pathak, R.; Chen, K.; Gurung, A.; Reza, K. M.; Bahrami, B.; Wu, F.; Chaudhary, A.; Ghimire, N.; Zhou, B.; Zhang, W. H. *Adv. Energy Mater.* 2019, *9* (36), 1901486.
(5) Chen, K.; Pathak, R.; Gurung, A.; Reza, K.; Ghimire, N.; Pokharel, J.; Baniya, A.; He, W.; Wu, J. J.; Qiao, Q. *J. Mater. Chem. A* 2020, *8*, 1911–1919.
(6) Chen, K.; Pathak, R.; Gurung, A.; Adhamash, E. A.; Bahrami, B.; He, Q.; Qiao, H.; Smirnova, A. L.; Wu, J. J.; Qiao, Q. *Energy Storage Mater.* 2019, *18*, 389–396.
(7) Wang, F.; Kim, S.-W.; Seo, D.-H.; Kang, K.; Wang, L.; Su, D.; Vajo, J. J.; Wang, J.; Graetz, J. *Nat. Commun.* 2015, *6* (1), 1–9.
(8) Prakash, R.; Mishra, A. K.; Roth, A.; Kübel, C.; Scherer, T.; Ghafari, M.; Hahn, H.; Fichtner, M. *J. Mater. Chem.* 2010, *20* (10), 1871–1876.
(9) Wu, F.; Srot, V.; Chen, S.; Lorger, S.; van Aken, P. A.; Maier, J.; Yu, Y. *Adv. Mater.* 2019, *31* (43), 1905146.
(10) Omenya, F.; Zagarella, N. J.; Rana, J.; Zhang, H.; Siu, C.; Zhou, H.; Wen, B.; Chernova, N. A.; Piper, L. F.; Zhou, G. *ACS Appl. Energy Mater.* 2019, *2* (7), 5243–5253.
(11) Fan, X.; Hu, E.; Ji, X.; Zhu, Y.; Han, F.; Hwang, S.; Liu, J.; Bak, S.; Ma, Z.; Gao, T. *Nat. Commun.* 2018, *9* (1), 1–12.
(12) Mäntymäki, M.; Ritala, M.; Leskelä, M. *Coatings* 2018, *8* (8), 277.
(13) Davis, V. K.; Bates, C. M.; Omichi, K.; Savoie, B. M.; Momčilović, N.; Xu, Q.; Wolf, W. J.; Webb, M. A.; Billings, K. J.; Chou, N. H. *Science* 2018, *362* (6419), 1144–1148.
(14) Gu, W.; Borodin, O.; Zdyrko, B.; Lin, H. T.; Kim, H.; Nitta, N.; Huang, J.; Magasinski, A.; Milicev, Z.; Berdichevsky, G. *Adv. Funct. Mater.* 2016, *26* (10), 1507–1516.
(15) Gmitter, A. J.; Badway, F.; Rangan, S.; Bartynski, R. A.; Halajko, A.; Pereira, N.; Amatucci, G. G. *J. Mater. Chem.* 2010, *20* (20), 4149–4161.
(16) Huang, Q.; Turcheniuk, K.; Ren, X.; Magasinski, A.; Song, A.-Y.; Xiao, Y.; Kim, D.; Yushin, G. *Nat. Mater.* 2019, *18* (12), 1343–1349.
(17) Thieu, D. T.; Fawey, M. H.; Bhatia, H.; Diemant, T.; Chakravadhanula, V. S. K.; Behm, R. J.; Kübel, C.; Fichtner, M. *Adv. Funct. Mater* 2017, *27* (31), 1701051.
(18) Liu, J.; Yuan, H.; Cheng, X.-B.; Chen, W.-J.; Titirici, M.-M.; Huang, J.-Q.; Yuan, T.; Zhang, Q. *Mater. Today Nano* 2019, *8*, 100049.
(19) Yan, K.; Wang, J.; Zhao, S.; Zhou, D.; Sun, B.; Cui, Y.; Wang, G. *Angew. Chem.* 2019, *131* (33), 11486–11490.

Electrode Sheets

Name	Composition	Purity	Nominal Voltage (V)	Capacity (minimum)	Capacity (nominal)	Cat. No.
Lithium manganese nickel oxide, LMNO	$Li_2Mn_3NiO_8$	≥98%	4.7 (Li/Li$^+$)	115 mAh/g	125 mAh/g	**765198-1EA**
Lithium manganese oxide, LMO	$LiMn_2O_4$	≥98%	4.7 (Li/Li$^+$)	110 mAh/g	120 mAh/g	**765201-1EA**
Lithium nickel cobalt aluminium oxide, NCA	$LiNi_{0.8}Co_{0.15}Al_{0.05}O_2$	≥98%	3.7 (Li/Li$^+$)	150 mAh/g	180 mAh/g	**765171-1EA**
Lithium nickel manganese cobalt oxide, NMC	$LiNi_{0.33}Mn_{0.33}Co_{0.33}O_2$	-	3.5 (Li/Li$^+$)	210 mAh/g	-	**765163-1EA**
Lithium titanate, LTO	$Li_4Ti_5O_{12}$	≥98%	1.5 (Li/Li$^+$)	160 mAh/g	150 mAh/g	**765155-1EA**

Cathode Materials

Name	Composition	Purity	Dimensions	Cat. No.
Cobalt monoantimonide	CoSb	99.9% trace metals basis	-80 mesh	**746320-5G**
Lithium cobalt(III) oxide	$LiCoO_2$	powder, 99.8% trace metals basis	-	**442704-100G-A**

Name	Composition	Purity	Dimensions	Cat. No.
Lithium cobalt phosphate, LCP	$LiCoPO_4$	powder, ≥99% (trace metals analysis)	-	**725145-25G**
Lithium iron(III) oxide	$LiFeO_2$	powder, 95%	particle size <1 μm	**442712-100G-A**
Lithium iron(II) phosphate, LFP	$LiFePO_4$	powder, >97% (XRF)	particle size <5 μm (BET)	**759546-5G**
Lithium manganese dioxide	$LiMnO_2$	powder, >99% trace metals basis	particle size <1 μm	**725137-25G**
Lithium manganese nickel oxide, LMNO	$Li_2Mn_3NiO_8$	powder, >99%	particle size <0.5 μm (BET)	**725110-25G**
Lithium manganese oxide, LMO	$LiMn_2O_4$	powder, >99%	particle size <0.5 μm (BET)	**725129-25G**
Lithium manganese(III,IV) oxide, LMO	$LiMn_2O_4$	-	particle size <5 μm	**482277-25G**
Lithium molybdate	Li_2MoO_4	powder or crystals, 99.9% trace metals basis	-	**400904-250G**
Lithium nickel cobalt aluminium oxide, NCA	$LiNi_{0.8}Co_{0.15}Al_{0.05}O_2$	powder, >98%	particle size <0.5 μm	**760994-10G**
Lithium nickel cobalt oxide, LNCO	$LiNi_{0.8}Co_{0.2}O_2$	powder, >98%	particle size <0.5 μm	**760986-10G**
Lithium nickel dioxide, LNO	$LiNiO_2$	powder, ≥98% trace metals basis	particle size <3 μm (BET)	**757365-10G**
Lithium nickel manganese cobalt oxide, NMC	$LiNi_{0.33}Mn_{0.33}Co_{0.33}O_2$	powder, >98%	particle size <0.5 μm	**761001-10G**

Anode Materials

Name	Purity	Description	Form	Cat. No.
Lithium	99%, metals basis	particle size 4 - 10 mesh	granular	**444456-10G** **444456-50G**
	99.9% trace metals basis	thickness × W 1.5 × 100 mm	ribbon	**266000-25G** **266000-100G**
	99.9% trace metals basis	thickness × W 0.75 × 45 mm	ribbon	**265993-25G** **265993-100G**
	99.9% trace metals basis	thickness × W 0.75 × 19 mm	ribbon	**320080-25G** **320080-100G**
	99.9% trace metals basis	thickness × W 0.38 × 23 mm	ribbon	**265985-25G** **265985-100G**
	≥98%	diam. 3.2 mm	wire	**278327-25G** **278327-100G**
Lithium-aluminum alloy	-	-	powder	**426490-25G**
Lithium titanate, LTO	-	−80 mesh	powder	**400939-100G**
Lithium titanate, spinel, LTO nanopowder	>99%	particle size <200 nm (BET)	nanopowder	**702277-25G**
Tin(IV) oxide	-	avg. part. size ≤100 nm	nanopowder	**549657-5G** **549657-25G**

Make Your Own Lithium-Ion Batteries

Applications of lithium-ion batteries (LIBs) extend from modern electronics to automobiles. Order ready-to-use electrolyte solutions and electrode sheets in battery grade to fabricate your LIB.
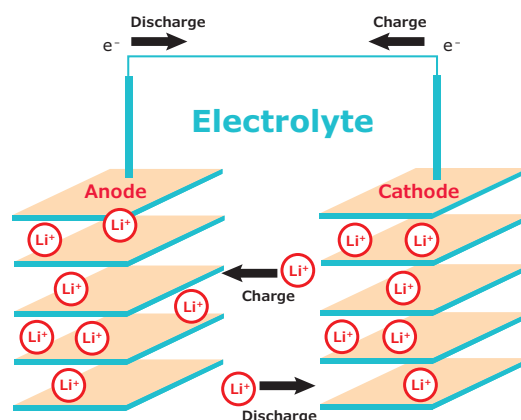
Electrolyte Solutions
H_2O < 15 ppm, HF < 50 ppm, APHA < 50

Name	Specifications	Cat. No.
2.0 M LiPF6 in EC/DMC=50/50 (v/v)	in ethylene carbonate and dimethyl carbonate	**809357**
2.0 M LiPF6 in EC/EMC=50/50 (v/v)	in ethylene carbonate and ethyl methyl carbonate	**809365**
2.0 M LiPF6 in EC/DEC=50/50 (v/v)	in ethylene carbonate and diethyl carbonate	**809349**
2.0 M LiPF6 in DMC	in dimethyl carbonate	**809411**
2.0 M LiPF6 in EMC	in ethyl methyl carbonate	**809403**
2.0 M LiPF6 in DEC	in diethyl carbonate	**809543**
2.0 M LiPF6 in PC	in propylene carbonate	**809470**

Electrode Sheets
Aluminum substrate, size 5 in. × 10 in.

| Name	Specifications	Composition	Cat. No.
Lithium nickel manganese cobalt oxide	loading >80%, thickness 25–50 μm	$LiNi_{0.33}Mn_{0.33}Co_{0.33}O_2$	**765163**
Lithium nickel cobalt aluminum oxide	loading >80%, thickness 12–25 μm	$LiNi_{0.8}Co_{0.15}Al_{0.05}O_2$	**765171**
Lithium manganese nickel oxide	loading >80%, thickness 25–50 μm	$Li_2Mn_3NiO_8$	**765198**
Lithium manganese oxide	loading >80%, thickness 25–40 μm	$LiMn_2O_4$	**765201**
Lithium titanate spinel	loading >80%, thickness 25–50 μm	$Li_4Ti_5O_{12}$	**765155**

To find out more, visit
SigmaAldrich.com/LIB

Recent Trends in Perovskite Solar Cells

Carlo Perini and Juan-Pablo Correa-Baena*

School of Materials Science and Engineering, Georgia Institute of Technology, Atlanta, Georgia, USA
*Email: jpcorrea@gatech.edu
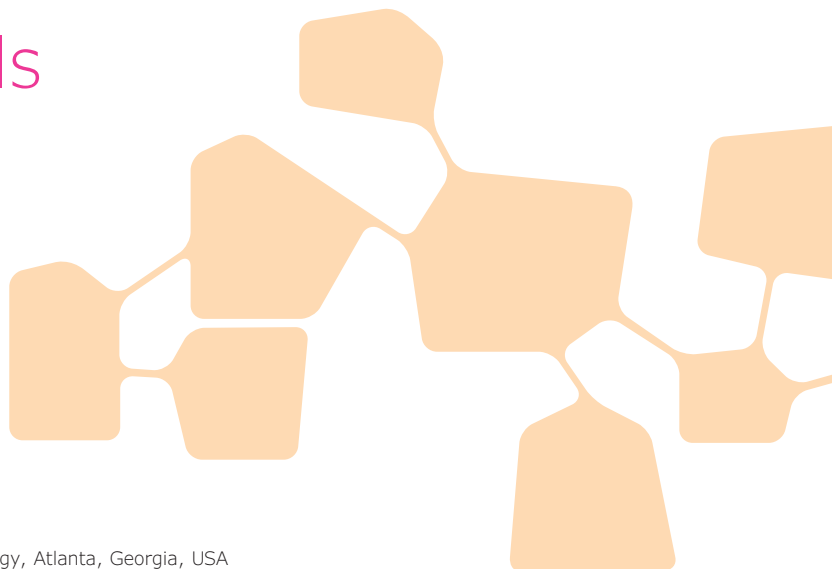
Introduction

Global energy demands are steadily increasing. Estimates vary, but energy demands are expected to rise by 30% to 800 exajoules by 2040, according to the Energy Information Administration.[1] Much of this demand could be supplied by the earth's most abundant renewable energy source, solar energy. If we consider that the earth includes vast areas that receive high levels of incident sunlight, including hot, arid deserts covering tens of millions of km^2, it is easy to envision that solar power has the potential to meet most, if not all, of our future energy requirements.[2] However, in order to harvest this vast potential energy source, it will be critical to maximize solar cell efficiency. In order to do this, we need to both apply the new technologies that have allowed approach the 33% theoretical performance limit in single-junction solar cells, and develop efficient and low-cost materials for multijunction photovoltaics.

Lead halide perovskite solar cells (PSC) are promising candidates for meeting our growing energy needs. Single-junction PSCs can achieve conversion efficiencies of above 25% using relatively simple and inexpensive deposition methods and low purity materials, an unprecedented feat for previous photovoltaic technology. This achievement is the result of electronic properties mostly unaffected by the presence of structural defects. The chemical composition and structure of perovskites can be easily modified in order to tune the bandgap of the material. Perovskites are significantly cheaper than any other wide bandgap alternative and thus carry promise to complement silicon in tandem structures. However, in order to achieve single-junction power conversion efficiencies (PCE) higher than 26%[3] PSCs require improvements to reduce non-radiative recombination. Similarly, their device long-term durability must

be improved. This will require development of standardized aging protocols complemented with data from field-testing of solar cells and panels.[4] Here, we discuss the latest efforts towards higher performance and stability of perovskite materials, both for single- and multi- junction solar cells.

Device Structure and State-of-the-Art

Lead halide perovskites, the most studied perovskite compositions to date, take on the 3D structure ABX$_3$. The A cation is methylammonium (MA), formamidinium (FA), Cs or Rb. Lead sits in the B site. The halides iodine, bromine or chlorine occupy the X site. A PSC is made of a perovskite active layer, electron and hole selective materials, and transparent and/or metal electrodes. The device structure nomenclature varies based on the location of electron collection. The direct or "n-i-p" terminology applies to PSCs where the electrons are collected at the transparent interface (bottom). The inverted or "p-i-n" terminology refers to solar cells that have electron/hole selective contacts flipped in the device stack (**Figure 1**). In a mesoporous structure, the bottom contact is porous: it is infiltrated and capped with perovskite material (**Figure 1A**). Finally, in a planar configuration all the layers tend to be compact thin films (**Figure 1B and C**).

PSC efficiencies increased rapidly during their first six years of development, swiftly reaching 20% and recently surpassing the 25% mark.[5] Researchers have now improved control of the deposition of perovskite films and engineered the bandgap and robustness of the material in single junctions via compositional engineering.[6–8] Using uniform and compact (>500 nm·thick)

perovskite films and a FA-based perovskite enabled efficiencies beyond 23% with currents approaching the theoretical limit.[9,10] PSCs show very high open-circuit voltages ($V_{OC's}$) compared to their bandgap, indicative of low recombination losses. Deposition, composition and device engineering have led to V_{OC} of up to 1.24 V at a bandgap of ≈1.6 eV, with a theoretical V_{OC} of 1.33 V for that bandgap.[3] Studies have shown that recombination dynamics at the perovskite/hole selective contact interface is largely responsible for the difference between theoretical and experimental $V_{OC's}$.[11] These findings prompted the study of perovskite surface passivation by 2D perovskite layers with bulky A-site cations.[9,12]

Early attempts at defect passivation at perovskite interfaces using thin films of wide bandgap materials enabled enhancement of the V_{OC} of a FA-based PSC, which helped to achieve a PCE of 23.2% (certified from current-voltage curve; 22.6% certified from the a stabilized current-voltage curve).[9] This achievement was followed by a report of a certified PCE of 23.3% from a stabilized current-voltage curve, warranting the exploration of new methods to identify and suppress recombination in order to boost this crucial PV parameter.[13]
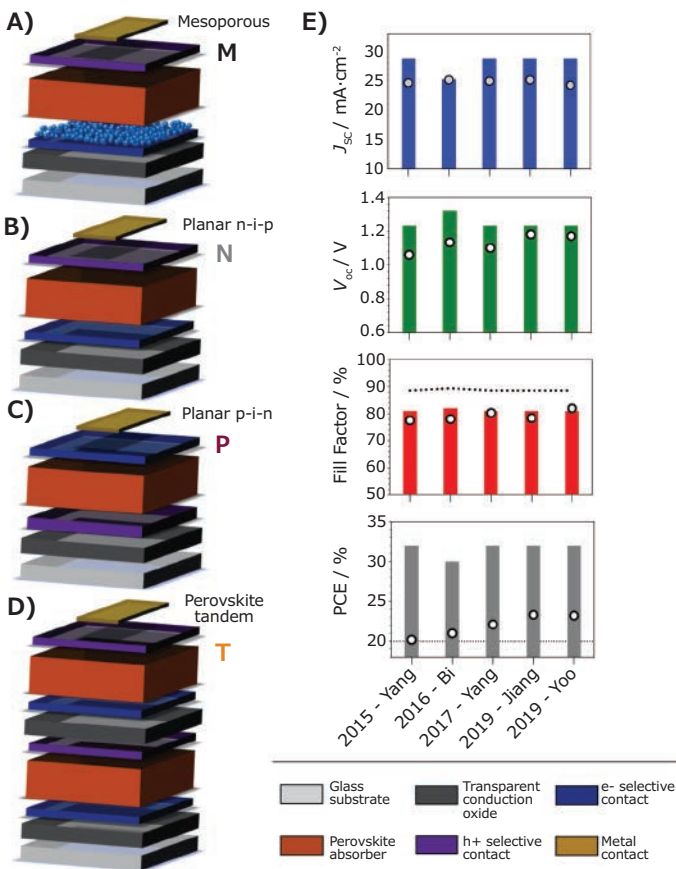
Compositional Engineering, Halide Segregation and Black Phase Stabilization

Stable 3D perovskite structures can be realized only by combining atoms with suitable steric hindrances. This requirement is quantified through the Goldschmidt tolerance factor (t), for which values between 0.8 and 1.0 result in stable 3D structures, such as in the case for MAPbI$_3$ (t ~ 0.9). Perovskites at the edge of the tolerance factor requirement, such as FAPbI$_3$ (t ~ 1) and CsPbI$_3$ (t ~ 0.8), have a strained 3D lattice. As a result, they tend to form lower dimensionality photo-inactive phases at room temperature.[16] Changes in the X anion have large impact on the bandgap value; increasing the Br content in an I perovskite increases the band gap closer to 1.7 eV—a value that is highly desired for perovskite/silicon tandems (**Figure 1D**). However, Br concentrations above 20% have raised concerns of halide segregation, possibly reducing device long-term stability and maximum V_{OC} by forming recombination-active impurities. Mixed Sn/Pb perovskites are promising for achieving optimal bandgaps in single junctions (1.1–1.4 eV, **Figure 2A**), but still suffer from significant losses due to recombination. The use of complex multi-cation and anion Pb formulations has enabled researchers to avoid photo-inactive phases and reduce halide segregation in the lattice.[17] A CsMAFA triple cation perovskite suppresses yellow phase impurities, even during crystallization, resulting in improved film performances regardless of annealing.[18] The introduction of the smaller rubidium in RbCsMAFA has enabled 21.6% stabilized PCEs with a 1.24 V Voc for a band gap of 1.63 eV, resulting in a loss-in-potential of 390mV—one of the lowest values ever reported for any solar cell material (**Figure 2B**).[6]

Figure 1. Schematics of perovskite solar cells based on the **A**) mesoporous and **B**) planar, with the conducting glass/electron contact/perovskite configuration (n-i-p). **C**) The inverted configuration (p-i-n) is a planar junction with a conducting glass/hole contact/perovskite stack. **D**) Perovskite-perovskite tandem device. **E**) Photovoltaic parameters of perovskite solar cells as calculated from Shockley-Queisser (bars) and metrics of selected publications (white circles) with certified efficiencies above 20% since 2015 and in chronological order to 2019.[3,9,12,14,15]
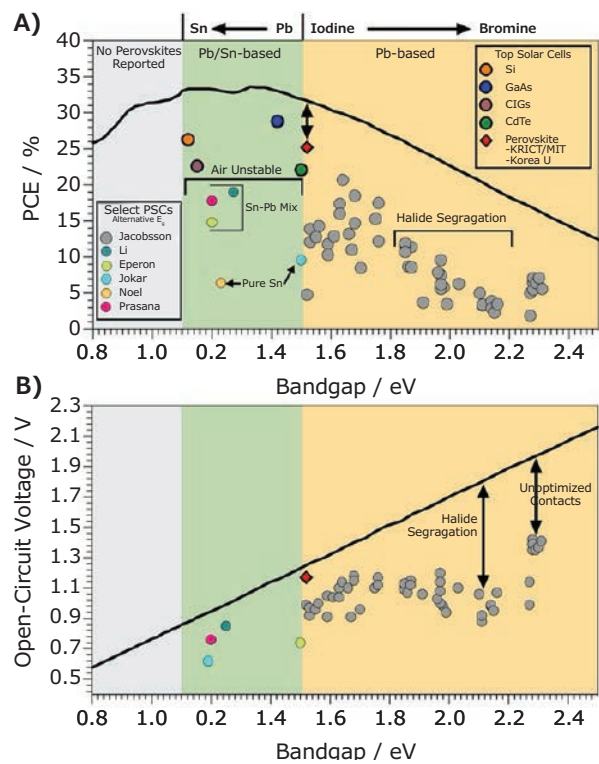

Figure 2. Device photophysics of state-of-the-art PSCs with **A**) Shockley Queisser efficiency and **B**) the calculated maximum V_{OC} (radiative limit) compared to values reached for different absorber materials.[5,21–26]

Following such examples, scientists have introduced other smaller cations, such as K, into solution without a clear explanation of how these positively charges atoms are incorporated; however, the presence of K^{+} clearly benefits the optoelectronic properties of the materials.[19] More recently the mechanism of how these cations are incorporated in the perovskite lattice has been studied, providing evidence of doping by strontium.[20] Cations larger than FA have been used to induce formation of lower dimensionality perovskite phases at interfaces, where the charge-transport layers are separated by the larger cations. Their larger bandgap enables passivation of surface defects, reducing non-radiative recombination and their use in devices has enabled current performance records.[9,12] Pure 2D/3D perovskites, where 2D interlayers are also diffused in the bulk, have been also reported. So far, the most stable and efficient perovskite compositions have been based on the combination of multi-cation perovskites and 2D interface passivation of 3D perovskites (**Figure 1E**).

Recombination and Passivation by 2D Perovskites

In a real device, bulk defects and surfaces/interfaces introduce recombination centers that result in rapid non-radiative recombination. Non-radiative recombination is different from radiative recombination and causes loss in potential (V_{OC} – bandgap/elementary charge, **Figure 2B**). While radiative recombination rate is a material property, non-radiative recombination is dictated by defects. Currently, interface recombination represents an obstacle for mixed-halide wide bandgap perovskites and for narrow bandgap tin-based perovskites used in multijunction solar cells stacks. Recent efforts allowed to significantly reduce interface recombination in single-junctions.[27] Bulk non-radiative recombination requires further reduction for all perovskite compositions. Lack of carrier selectivity, barriers to charge extraction and surface defects at interfaces are main causes of surface recombination. Other research has reported non-radiative recombination at grain boundaries in perovskite films, along specific crystallographic facets, and in the presence of porosity in the film, although this still remains a debated topic.[28] Bulk recombination in PSCs has been attributed to electron-phonon coupling, band electronic disorder (higher Urbach energy) and deep-defects (both intrinsic and induced by impurities). To reach $V_{OC,rad}$, and in turn, to also maximize the FF to nearly 90%, investigators will need to minimize the impact of such defects, with the goal of approaching 10 μs non-radiative lifetimes.[27]

PSC Stability: Requirements and Achievements

The key cost drivers of new solar technology include capital expenditures as well as energy yield, which is a product of device efficiency and long-term stability. The degradation of the PCE over time controls the return on investment and thus, the risks associated with a new PV technology. The market reference for solar technology is crystalline silicon, with a degradation rate below 0.5% per year, delivering performance for 25 years under operational conditions. PSCs must reach similar levels of stability to compete within the photovoltaic market.

A significant body of research has been devoted to this aim in the last few years, with significant efforts directed to reducing the impact on stability of both intrinsic and extrinsic degradation factors. Despite initial scepticism, perovskite solar cells can now withstand the damp-heat and temperature-cycling protocols used for accelerated aging in the silicon industry (IEN6125).[29] Milestones in this progress have provided effective design of each of the device layers and interfaces, and the development of effective encapsulation techniques.[29] The impact of extrinsic degradation factors, such as temperature, or chemically active species as humidity and oxygen, and the release of perovskite degradation by-products have been minimized, halting further material degradation.[29,30] More recently, inorganic device structures have started to attract attention: a stable photovoltaic β-phase has been discovered at room temperature for $CsPbI_3$, raising efficiencies above 10%. Combined with inorganic interlayers, such compositions promise to overcome the low-stability issue of perovskite photovoltaics.[30]

PSC Stability: Aging Protocols and Field Testing

Perovskites fall subject to ion migration, which partake in both fast (seconds to minutes) and slow (minutes to hours) performance degradation, namely hysteresis and reversible losses (**Figure 3A-D**). In the latter, devices suffer from decreased PCE during aging and recover to the initial value after dark storage for a few hours. Consequently, a true estimation of device lifetime becomes complex, and easily prone to over or under estimation. Even simple figures of merit as T80 can be misleading, depending on how they are reported. Regardless, establishing how organic and inorganic contacts affect the accumulation of ions in the long term proves critical, as mild, reversible losses does not guarantee long-term stability. Suitable characterization protocols need to be developed to correlate stress factors and device degradation, to enable further improve device stability. Following the example of organic photovoltaics, researchers have attempted to craft characterization guidelines for perovskite devices by complementing the International Summit on Organic Photovoltaic Stability (ISOS) protocols with further measurements aimed at assessing the impact of ionic motion on device stability. They further defined reporting standards to truly enable the implementation of round robin experiments on published devices. A formatted reporting of such data, their integration in databases, and their correlation through machine learning algorithms, would contribute to a better understanding of the current limiting factors for device stability.[31] As the field develops, more field-testing data from solar cells and panels are expected to be published. The study of the observed failure mechanisms and their correlation with the ones observed in the accelerated aging protocols will enable further improve the aging standards and to correlate such results with expected device lifetimes.[31]
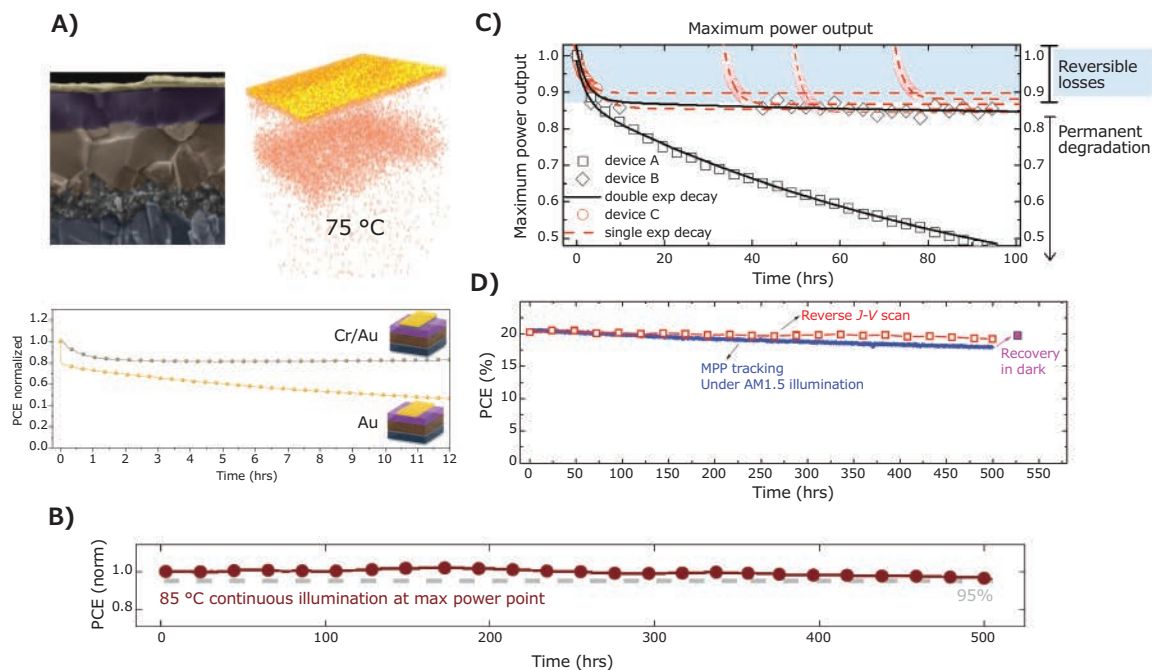
Figure 3. Long-term stability of perovskite solar cells. A) Gold migration-induced PCE degradation under light, maximum power point and 75 °C. It can be offset by a Cr interlayer between Spiro-OMeTAD and the gold electrode.[32] B) The use of multiple cations and a PTAA hole contact shows losses around 5% in 500hrs of MPP tracking at 85 °C, in a mesoporous device.[33] C) Maximum power output in real working conditions shows reversible losses before going through permanent degradation.[34] D) One of the most stable planar devices exhibited losses around 10% in 500 hrs of MPP tracking at room temperature.[35]
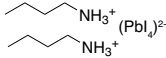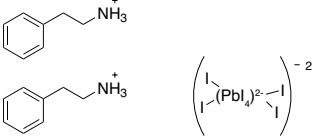
Promises and Challenges

PSCs have made remarkable advances in just a few years — a result of both the scientific community's extensive efforts and expertise developed in more established fields, such as organic or dye-sensitized solar cells. The above 25% lab-scale efficiency and the remarkably low loss-in-potential recently reported by PSCs show that these solution-processed solar cells are ready to rival other state-of-the-art technologies, such as Si or GaAs. Having reached the single-junction efficiency target, the focus of the perovskite community has now shifted towards tandem solar cells and long-term stability. The perovskite community is trying to develop testing protocols able to account for the unique dynamics of these materials. First reports simulating outdoor field-testing have recently been published, but more data are required to provide statistical robustness and to confirm the validity of the proposed aging protocols.[36] To become a player in the energy market, PSCs must be able to last for at least 20 years with minimal degradation. Scientists can only accomplish this task by mitigating intrinsic and extrinsic degradation due to ion migration in the perovskite device stack.

References

(1) International Energy Outlook 2019, https://www.eia.gov/outlooks/ieo/, (accessed 13 May 2020).
(2) Moriarty, P.; Honnery, D. *Sustain. Energy Rev.* **2012**, *16*, 244–252.
(3) Correa-Baena, J.-P.; Saliba, M.; Buonassisi, T.; Grätzel, M.; Abate, A.; Tress, W.; Hagfeldt, A. *Science* **2017**, *358*, 739–744.
(4) Saliba, M.; Correa-Baena, J.-P.; Grätzel, M.; Hagfeldt A.; Abate, A. *Angew. Chemie Int. Ed.* **2018**, *57*, 2554–2569.
(5) NREL, Best Research- Cell Efficiencies - 2020/05/13, https://www.nrel.gov/pv/cell-efficiency.html.
(6) Saliba, M.; Matsui, T.; Domanski, K.; Seo, J.-Y.; Ummadisingu, A.; Zakeeruddin, S. M.; Correa-Baena, J.-P.;. Tress, W. R; Abate, A.; Hagfeldt, A.; Grätzel, M. *Science*, **2016**, *354*, 206–209.
(7) Jeon, N. J.; Noh, J. H.; Yang, W. S.; Kim, Y. C.; Ryu, S.; Seo, J.; Seok, S. I. *Nature* **2015**, *517*, 476–480.
(8) Turren-Cruz, S.-H.; Hagfeldt, A.; Saliba, M. *Science* **2018**, *362*, 449–453.
(9) Yoo, J. J.; Wieghold, S.; Sponseller, M. C.; Chua, M. R.; Bertram, S. N.; Hartono, N. T. P.; Tresback, J. S.; Hansen, E. C.; Correa-Baena, J.-P.; Bulović, V.; Buonassisi, T.; Shin, S. S.; Bawendi, M. G. *Energy Environ. Sci.* **2019**, *12*, 2192–2199.
(10) Correa-Baena, J.-P.; Anaya, M.; Lozano, G.; Tress, W.; Domanski, K.; Saliba, M.; Matsui, T.; Jacobsson, T. J.; Calvo, M. E.; Abate, A.; Grätzel, M.; Míguez, H.;Hagfeldt, A. *Adv. Mater.* **2016**, *28*, 5031–5037.
(11) Correa-Baena, J.-P.; Tress, W.; Domanski, K.; Anaraki, E. H.; Turren-Cruz, S.-H.; Roose, B.; Boix, P. P.; Grätzel, M.; Saliba, M.; Abate, A.; Hagfeldt, A. *Energy Environ. Sci.* **2017**, *10*, 1207–1212.
(12) Jiang, Q.; Zhao, Y.; Zhang, X.; Yang, X.; Chen, Y.; Chu, Z.; Ye, Q.; Li, X.; Yin, Z.; You, J. *Nat. Photonics* DOI:10.1038/s41566-019-0398-2.
(13) Jiang, Q.; Zhao, Y.; Zhang, X.; Yang, X.; Chen, Y.; Chu, Z.; Ye, Q.; Li, X.; Yin, Z.; You, J. *Nat. Photonics*, **2019**, *13*, 460–466.
(14) Yang, W. S.; Noh, J. H.; Jeon, N. J.; Kim, Y. C.; Ryu, S.; Seo, J.; Seok, S. I. **2015**, 1–12.
(15) Bi, D.; Yi, C.; Luo, J.; Décoppet, J.-D.; Zhang, F.; Zakeeruddin, S. M.; Li, X.; Hagfeldt, A.; Grätzel, M. *Nat. Energy* **2016**, *1*, 16142.
(16) Goldschmidt, V. M. *Naturwissenschaften* **1926**, *14*, 477–485.
(17) Correa-Baena, J.-P.; Luo, Y.; Brenner, T. M.; Snaider, J.; Sun, S.; Li, X.; Jensen, M. A.; Hartono, N. T. P.; Nienhaus, L.; Wieghold, S.; Poindexter, J. R.; Wang, S.; Meng, Y. S.; Wang, T.; Lai, B.; Holt, M. V; Cai, Z.; Bawendi, M. G.; Huang, L.; Buonassisi, T.; Fenning, D. P. *Science* **2019**, *363*, 627–631.
(18) Saliba, M.; Matsui, T.; Seo, J.-Y.; Domanski, K.; Correa-Baena, J.-P.; Nazeeruddin, M. K.; Zakeeruddin, S. M.; Tress, W.; Abate, A.; Hagfeldt, A.; Grätzel, M. *Energy Environ. Sci.* **2016**, *9*, 1989–1997.
(19) Abdi-Jalebi, M.; Andaji-Garmaroudi, Z.; Cacovich, S.; Stavrakas, C.; Philippe, B.; Richter, J. M.; Alsari, M.; Booker, E. P.; Hutter, E. M.; Pearson, A. J.; Lilliu, S.; Savenije, T. J.; Rensmo, H.; Divitini, G.; Ducati, C.; Friend, R. H.; Stranks, S. D. *Nature* **2018**, *555*, 497–501.
(20) Phung, N.; Felix, R.; Meggiolaro, D.; Al-ashouri, A.; Sousa, G.; Hartmann, C.; Hidalgo, J.; Kobler, H.; Mosconi, E.; Lai, B.; Gunder, R.; Li, M.; Wang, K.; Wang, Z.; Nie, K.; Handick, E.; Wilks, R. G.; Marquez, J. A.; Rech, B.; Unold, T.; Correna-Baena, J.-P.; Albrecht, S.; De Angelis, F.; Bar, M.; Abate, A. *J. Am. Chem. Soc.* **2020**, *142* (5), 2365–2374. DOI:10.1021/jacs.9b11637.

(21) Jesper Jacobsson, T.; Correa-Baena, J.-P.; Pazoki, M.; Saliba, M.; Schenk, K.; Gratzel, M.; Hagfeldt, A. *Energy Environ. Sci.* **2016**, *9*, 1706–1724.

(22) Li, C.; Song, Z.; Zhao, D.; Xiao, C.; Subedi, B.; Shrestha, N.; Junda, M. M.; Wang, C.; Jiang, C. S.; Al-Jassim, M.; Ellingson, R. J.; Podraza, N. J.; Zhu, K.; Yan, Y. *Adv. Energy Mater.*, **2019**, *9*, 1803135.

(23) deQuilettes, D. W.; Vorpahl, S. M.; Stranks, S. D.; Nagaoka, H.; Eperon, G. E.; Ziffer, M. E.; Snaith, H. J.; Ginger, D. S. *Science* **2015**, *348*, 683–686.

(24) Eperon, G. E.; Leijtens, T.; Bush, K. A.; Prasanna, R.; Green, T.; Wang, J. T. W.; McMeekin, D. P.; Volonakis, G.; Milot, R. L.; May, R.; Palmstrom, A.; Slotcavage, D. J.; Belisle, R. A.; Patel, J. B.; Parrott, E. S.; Sutton, R. J.; Ma, W.; Moghadam, F.; Conings, B.; Babayigit, A.; Boyen, H. G.; Bent, S.; Giustino, F.; Herz, L. M.; Johnston, M. B.; McGehee, M. D.; Snaith, H. J. *Science* **2016**, *354*, 861–865.

(25) Brenes, R.; Guo, D.; Osherov, A.; Noel, N. K.; Eames, C.; Hutter, E. M.; Pathak, S. K.; Niroui, F.; Friend, R. H.; Islam, M. S.; Snaith, H. J.; Bulović, V.; Savenije, T. J.; Stranks, S. D. *Joule* **2017**, *1* (1), 155–167. DOI:10.1016/j.joule.2017.08.006.

(26) Noel, N. K.; Stranks, S. D.; Abate, A.; Wehrenfennig, C.; Guarnera, S.; Haghighirad, A. A.; Sadhanala, A.; Eperon, G. E.; Pathak, S. K.; Johnston, M. B.; Petrozza, A.; Herz, L. M.; Snaith, H. J. *Energy Environ. Sci.* **2014**, *7*, 3061–3068.

(27) Luo, D. *Nat. Rev. Mater.* **2020**, *5*, 16–19.

(28) Castro-Méndez, A.; Hidalgo, J.; Correa-Baena, J. *Adv. Energy Mater.* **2019**, *9* (38), 1901489.

(29) Cheacharoen, R.; Boyd, C. C.; Burkhard, G. F.; Leijtens, T.; Raiford, J. A.; Bush, K. A.; Bent, S. F.; McGehee, M. D. *Sustain. Energy Fuels* **2018**, *2*, 2398–2406.

(30) Wang, Q.; Phung, N.; Di Girolamo, D.; Vivo, P.; Abate, A. *Energy Environ. Sci.* **2019**, *12*, 865–886. DOI:10.1039/C8EE02852D.

(31) Khenkin, M. V; Katz, E. A.; Abate, A.; Bardizza, G.; Berry, J. J.; Brabec, C.; Brunetti, F.; Bulović, V.; Burlingame, Q.; Di Carlo, A.; Matheron, M.; Mcgehee, M.; Meitzner, R.; Nazeeruddin, M. K., et. al. *Nat. Energy* **2020**, 5, 35–49. DOI:10.1038/s41560-019-0529-5.

(32) Domanski, K.; Correa-Baena, J.-P.; Mine, N.; Nazeeruddin, M. K.; Abate, A.; Saliba, M.; Tress, W.; Hagfeldt, A.; Grätzel, M. *ACS Nano* **2016**, *10* (6), 6306–6314. DOI:10.1021/acsnano.6b02613.

(33) Saliba, M.; Matsui, T.; Domanski, K.; Seo, J.-Y.; Ummadisingu, A.; Zakeeruddin, S. M.; Correa-Baena, J.-P.; Tress, W. R.; Abate, A.; Hagfeldt, A.; Grätzel, M. *Science* **2016**, *354*, 206–209.

(34) Domanski, K.; Roose, B.; Matsui, T.; Saliba, M. Turren-Cruz,; Correa-Baena, J.-P.; Carmona, C. R.; Richardson, G.; Foster, J. M.; De Angelis, F.; Ball, J. M.; Petrozza, A.; Mine, N.; Nazeeruddin, M. K.; Tress, W.; Grätzel, M.; Steiner, U.; Hagfeldt, A.; Abate, A. *Energy Environ. Sci.* **2017**, *10*, 604–613.

(35) Stolterfoht, M.; Wolff, C. M.; Amir, Y.; Paulke, A.; Perdigón-Toro, L.; Caprioglio, P.; Neher, D. *Energy Environ. Sci.* **2017**, *10*, 1530–1539.

(36) Tress, W.; Domanski, K.; Carlsen, B.; Agarwalla, A.; Alharbi, E. A.; Graetzel, M.; Hagfeldt, A. *Nat. Energy* **2019**, *4*, 568–574. DOI:10.1038/s41560-019-0400-8.

2D Perovskites

Name	Structure	Cat. No.
Di-*n*-butylammonium tetraiodoplumbate		910961-1G 910961-2.5G
Bis[(2-phenylethyl)ammonium] tetraiodoplumbate		910937-1G 910937-2.5G

Precursors for Organometallic Perovskites

Organohalide Materials

Name	Composition	Form	Purity	Cat. No.
Acetamidinium iodide	$C_2H_7IN_2$	powder	98%	805971-5G 805971-25G
Benzylammonium bromide	$C_7H_{10}BrN$	powder or crystals	≥98%	900885-5G 900885-25G
Benzylammonium iodide	$C_7H_{10}IN$	powder	98%	806196-5G 806196-25G
Bis[4-(glycidyloxy)phenyl] methane	$C_{19}H_{20}O_4$	liquid or solid	>88%	900198-100ML
n-Butylammonium bromide	$C_4H_{12}BrN$	powder or crystals	≥98%	900817-10G 900817-25G
t-Butylammonium bromide	$C_4H_{12}BrN$	powder or crystals	≥98%	900827-10G 900827-25G
i-Butylammonium bromide	$C_4H_{12}BrN$	powder or crystals	-	900869-10G 900869-25G
n-Butylammonium iodide	$C_4H_{12}IN$	powder	98%	805874-5G 805874-25G

Name	Composition	Form	Purity	Cat. No.
t-Butylammonium iodide	$C_4H_{12}IN$	powder	98%	**806102-5G** **806102-25G**
i-Butylammonium iodide	$C_4H_{12}IN$	powder	98%	**805866-5G** **805866-25G**
Diethylammonium bromide	$(C_2H_5)_2NH \cdot HBr$	powder or crystals	≥98%	**900840-10G** **900840-25G**
Diethylammonium iodide	$C_4H_{12}IN$	powder	98%	**806188-5G** **806188-25G**
Dimethylammonium bromide	C_2H_8BrN	powder	≥98%	**900872-10G** **900872-25G**
Dimethylammonium iodide	C_2H_8IN	powder	98%	**805831-5G** **805831-25G**
Ethane-1,2-diammonium bromide	$C_2H_{10}Br_2N_2$	powder	≥98%	**900833-5G** **900833-25G**
Ethane-1,2-diammonium iodide	$C_2H_8N_2 \cdot 2HI$	powder or crystals	≥98%	**900852-5G** **900852-25G**
Formamidinium bromide	CH_5BrN_2	powder or crystals	≥98%	**900835-5G** **900835-25G**
	CH_5BrN_2	powder or crystals	≥99%	**901437-10G**
Formamidinium iodide	CH_5IN_2	powder	≥99%	**901436-10G**
	CH_5IN_2	powder	≥98%, H-NMR	**806048-5G** **806048-25G**
Guanidinium bromide	CH_6BrN_3	powder or crystals	≥98%	**900839-10G** **900839-25G**
	CH_6BrN_3	powder	≥99%	**901452-10G**
Guanidinium iodide	CH_6IN_3	powder	≥99%	**806056-5G** **806056-25G**
	CH_6IN_3	powder	≥99%	**901450-10G**
Imidazolium bromide	$C_3H_4N_2 \cdot HBr$	powder	≥98%	**900821-5G** **900821-25G**
Imidazolium iodide	$C_3H_5IN_2$	powder	98%	**805963-25G**
Methylammonium bromide	CH_6BrN	powder	98%	**806498-25G**
	CH_6BrN	powder	≥99%	**901435-10G**
	$CH_3NH_2 \cdot HBr$	powder	98%	**793507-5G**
Methylammonium bromide solution	-	0.18 M in 2-propanol	-	**808407-50ML**
Methylammonium chlorodiiodoplumbate(II) precursor solution	CH_6NClI_2Pb	liquid	-	**809039-25G**
Methylammonium iodide	$CH_3NH_2 \bullet HI; C_6H_6IN$	powder	98%	**793493-5G**
	$CH_3NH_2 \bullet HI; C_6H_6IN$	powder	-	**806390-25G**
	CH_6IN	crystals	≥99%	**901434-10G**
Methylammonium triiodoplumbate(II) precursor solution	$[CH_3NH_3]^+[PbI_3]^-$	40 wt. % in DMF	-	**793833-5ML**
Phenethylammonium bromide	$C_8H_{12}BrN$	powder or crystals	≥98%	**900829-10G** **900829-25G**
Phenethylammonium iodide	$C_8H_{12}IN$	powder	98%	**805904-25G**
Phenylammonium bromide	C_6H_8BrN	powder or crystals	≥98%	**900828-10G** **900828-25G**
Phenylammonium iodide	C_6H_8IN	powder	≥98%, H-NMR	**805912-5G** **805912-25G**
Propane-1,3-diammonium bromide	$C_3H_{12}Br_2N_2$	powder or crystals	≥98%	**900834-5G** **900834-25G**
Propane-1,3-diammonium iodide	$C_3H_{12}I_2N_2$	powder	≥98%	**900832-5G** **900832-25G**
n-Propylammonium bromide	$C_3H_{10}BrN$	powder or flakes	≥98%	**900819-10G** **900819-25G**
i-Propylammonium bromide	$C_3H_{10}BrN$	powder or crystals	≥98%	**900816-10G** **900816-25G**
n-Propylammonium iodide	$C_3H_{10}IN$	powder	-	**805858-5G** **805858-25G**
i-Propylammonium iodide	$C_3H_{10}IN$	powder	98%	**805882-5G** **805882-25G**
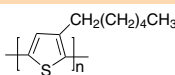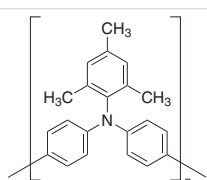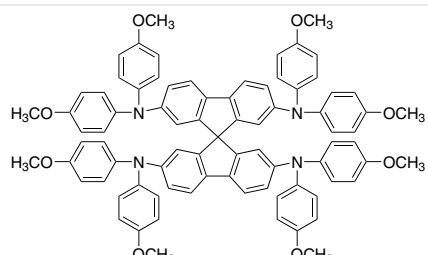
Lead Halides

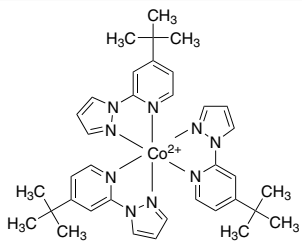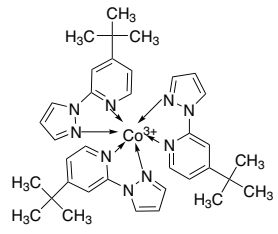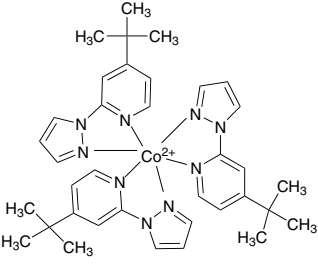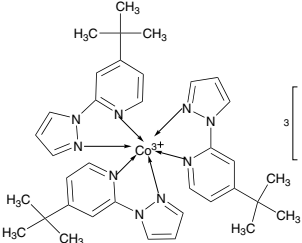| Name	Composition	Form	Purity	Cat. No.
Lead(II) bromide	PbBr$_2$	powder	99.999% trace metals basis	**398853-5G**
	PbB	powder	≥98%	**211141-100G** **211141-500G**
Lead(II) chloride	PbCl$_2$	beads	99.999%	**449865-5G**
	PbCl$_2$	powder and chunks	99.999% trace metals basis	**203572-10G** **203572-50G**
	PbCl$_2$	powder	98%	**268690-5G** **268690-250G** **268690-1KG**
Lead(II) iodide	PbI$_2$	beads	99.999% trace metals basis	**554359-5G**
	PbI$_2$	solid	99.999% trace metals basis	**203602-50G**
	PbI$_2$	powder	99%	**211168-50G**
Lead(II) iodide solution	PbI$_2$	0.55 M in DMF	-	**795550-10ML**
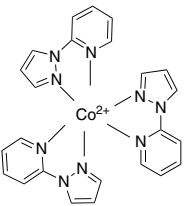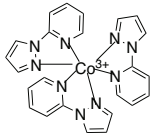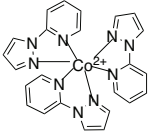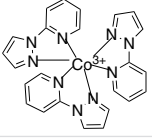
Titania Nanomaterials for Support
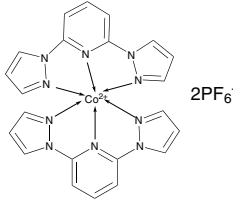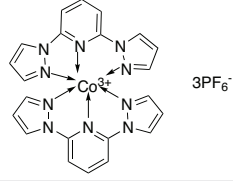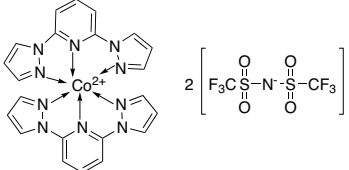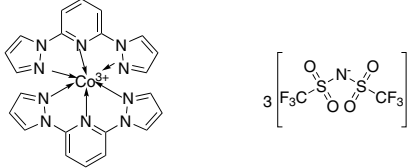
Name	Description	Purity	Form	Cat. No.
Titanium	particle size <100 nm	98.5% trace metals basis	dispersion nanoparticles	**513415-5G**
Titanium dioxide	particle size 22 nm & >150 nm (BET), spec. surface area 50-60 m^2/g (BET)	-	paste (nanocrystalline colloid)	**798517-25G**
	average diameter 25 nm	-	nanotubes powder	**799289-500MG**
Titanium(IV) oxide	primary particle size 21 nm (TEM), surface area 35-65 m^2/g (BET)	≥99.5% trace metals basis	nanopowder	**718467-100G**
Titanium(IV) oxide, anatase	particle size <25 nm, spec. surface area 45-55 m^2/g	99.7% trace metals basis	nanopowder	**637254-50G** **637254-100G** **637254-500G**
Titanium(IV) oxide, mixture of rutile and anatase	particle size <50 nm (XRD) particle size <100 nm (BET)	99.5% trace metals basis	nanopowder	**634662-25G** **634662-100G**
	particle size <250 nm (DLS) particle size ~21 nm (primary particle size of starting nanopowder)	99.9% trace metals basis	nanoparticle paste	**700355-25G**
	particle size <150 nm (volume distribution, DLS) particle size ~21 nm (primary particle size of starting nanopowder)	99.5% trace metals basis	dispersion nanoparticles	**700347-25G** **700347-100G**
	particle size <100 nm particle size ~30 nm (primary particle size of starting nanopowder)	99.9% trace metals basis	dispersion nanoparticles	**700339-100G**
Titanium(IV) oxide, rutile	particle size <100 nm, spec. surface area 50 m^2/g	99.5% trace metals basis	nanopowder	**637262-25G** **637262-100G** **637262-500G**

Hole Transport Materials (HTM)

Name	Structure	Purity/Molecular Weight	Cat. No.
Poly(3-hexylthiophene-2,5-diyl)		average M$_w$ 20,000-45,000	**900563-1G** **900563-5G**
		average M$_w$ 50,000-75,000	**900550-1G** **900550-5G**
		average M$_w$ 85,000-100,000	**900549-1G**
		average M$_w$ 50,000-100,000	**445703-1G**
PTAA		average M$_n$ 7,000-10,000 (GPC)	**702471-100MG** **702471-1G**
Spiro-MeOTAD		99%, HPLC	**792071-1G** **792071-5G**

Hole Conductor Cobalt Dopants

Name	Structure	Purity	Cat. No.
FK 102 Co(II) PF$_6$ salt	• 2 PF$_6^-$	98%	**805238-5G**
FK 102 Co(III) PF$_6$ salt	3PF$_6^-$	>98%	**805254-5G**
FK 102 Co(II) TFSI salt	$2\left[F_3C-\overset{O}{\underset{O}{S}}-N-\overset{O}{\underset{O}{S}}-CF_3 \right]$	98%	**805246-5G**
FK 102 Co(III) TFSI salt	$3\left[F_3CS-N^-\overset{O}{\underset{O}{S}}-CF_3 \right]$	98%	**805203-5G**
FK 209 Co(II) PF$_6$ salt	• 2PF$_6^-$	98%	**805378-5G**
FK 209 Co(III) PF$_6$ salt	• 3PF$_6^-$	98%	**805408-5G**
FK 209 Co(II) TFSI salt	$2\left[F_3C-\overset{O}{\underset{O}{S}}-N^-\overset{O}{\underset{O}{S}}-CF_3 \right]$	98%	**805386-5G**
FK 209 Co(III) TFSI salt	$3\left[F_3CS-N^-\overset{O}{\underset{O}{S}}-CF_3 \right]$	98%	**805394-5G**

Name	Structure	Purity	Cat. No.
FK 269 Co(II) PF$_6$ salt	2PF$_6$$^-$	98%	**805548-5G**
FK 269 Co(III) PF$_6$ salt	3PF$_6$$^-$	98%	**805521-5G**
FK 269 Co(II) TFSI salt	$2\left[F_3CS-N^-S-CF_3\right]$	98%	**805815-5G**
FK 269 Co(III) TFSI salt	$3\left[F_3CS-N^-S-CF_3\right]$	98%	**805807-5G**

Fluorine-Doped Tin Oxide (FTO) Coated Glass

Surface Resistivity (Ω/sq)	Haze	Transmittance	L × W × D (mm)	Cat. No.
~7	5%	80-82% (visible)	50 × 50 × 2.2	**735140-5EA**
	5%	80-82% (visible)	100 × 100 × 2.3	**735159-5EA**
	5%	80-82% (visible)	300 × 300 × 2.2	**735167-1EA**
~8	12%	80-81.5% (visible)	50 × 50 × 3	**735175-5EA**
	12%	80-81.5% (visible)	100 × 100 × 3	**735183-5EA**
	12%	80-81.5% (visible)	300 × 300 × 3.2	**735191-1EA**
~10	1%	83% (visible)	50 × 50 × 3	**735205-5EA**
	1%	83% (visible)	100 × 100 × 3	**735213-5EA**
	1%	83% (visible)	300 × 300 × 3	**735221-1EA**
~13	≤0.74%	82-84.5% (visible)	50 × 50 × 2.2	**735248-5EA**
	≤0.74%	82-84.5% (visible)	100 × 100 × 2.2	**735256-5EA**
	≤0.74%	82-84.5% (visible)	300 × 300 × 2.3	**735264-1EA**

2D Layered Perovskites

Solution Processable Materials

The recent discovery that single-layer 2D perovskites can be prepared using solution processing techniques[1] has been followed by enormous research into optoelectronic applications of 2D perovskites including light emitting diodes (LEDs),[2] phototransistors,[3] and solar cells,[4] and lasers.[5]

Direct and Tunable Bandgap

Photoluminescent 2D perovskites have a direct bandgap with a narrow emission peak that changes depending on the layer thickness and the choice of amine and halide. We offer an excellent portfolio of the most popular 2D perovskite compositions for photoluminescence based devices.

Improved Moisture Stability

Solar cells fabricated with 2D perovskites have improved stability in moist air compared to 3D perovskites.[4]

Formula	Cat. No.	Layer Thickness	$(RNH_3)_2(MeNH_3)_{n-1}Pb_nX_{3n+1}$		
			R	X	n
$(BA)_2PbI_4$	**910961**	n=1	Bu	I	1
$(BA)_2PbBr_4$	**910953**	n=1	Bu	Br	1
$(PEA)_2PbI_4$	**910937**	n=1	PE	I	1
$(PEA)_2PbBr_4$	**910945**	n=1	PE	Br	1
$(BA)_2(MA)Pb_2I_7$	**912816**	n=2	Bu	I	2
$(BA)_2(MA)_2Pb_3I_{10}$	**912557**	n=3	Bu	I	3
$(BA)_2(MA)_3Pb_4I_{13}$	**914363**	n=4	Bu	I	4
$(BA)_2(MA)_4Pb_5I_{16}$	**912301**	n=5	Bu	I	5

BA = n-butylammonium; PEA = 2-phenylethylammonium;
MA =methylammonium, Bu=n-butyl, PE=2-phenylethyl

SigmaAldrich.com/perovskite

References:

1) Dou, L.; Wong, A. B.; Yu, Y.; Lai, M.; Kornienko, N.; Eaton, S. W.; Fu, A.; Bischak, C. G.; Ma, J.; Ding, T.; Ginsberg, N. S.; Wang, L-W.; Alivisatos, A. P.; Yang, P. *Science* **2015,** *349,* 1518. DOI: 10.1126/science.aac7660

2) Yuan, M.; Quan, L. N.; Comin, R.; Walters, G.; Sabatini, R.; Voznyy, O.; Hoogland, S.; Zhao, Y.; Beauregard,E. M.; Kanjanaboos, P.; Lu, Z.; Kim, D. H.; Sargent, E. H. *Nat. Nanotechnol.* **2016,** *11,* 872. DOI: 10.1038/NNANO.2016.110

3) Shao, Y.; Liu, Y.; Chen, X.; Chen, C.; Sarpkaya, I.; Chen, Z.; Fang, Y.; Kong, J.; Watanabe, K.;Taniguchi, T.; Taylor, A.; Huang, J.; Xia, F. *Nano Lett.* **2017,** *17,* 7330. DOI: 10.1021/acs.nanolett.7b02980

4) Cao, D. H.; Stoumpos, C. C.; Farha, O. K.; Hupp, J. T.; Kanatzidis, M. G. *J. Am. Chem.* Soc. **2015,** *137,* 7843. DOI: 10.1021/jacs.5b03796

5) Raghavan, C. M.; Chen, T.-P.; Li, S.-S.; Chen, W.-L.; Lo, C.-Y.; Liao, Y.-M.; Haider, G.; Lin, C.-C.; Chen, C.-C.; Sankar, R.; Chang, Y.-M.; Chou, F.-C.; Chen, C.-W. *Nano Lett.* **2018,** *18* (5), 3221. DOI: 10.1021/acs.nanolett.8b00990

Recent Advances in Solid-State Rechargeable Batteries

Chunwen Sun[1,2]*

[1] CAS Center for Excellence in Nanoscience, Beijing Institute of Nanoenergy and Nanosystems, Chinese Academy of Sciences, Beijing 100083, China
[2] School of Nanoscience and Technology, University of Chinese Academy of Sciences, Beijing 100049, China
* E-mail: sunchunwen@binn.cas.cn

Introduction

Lithium-ion batteries (LIBs) have been considered the most promising energy storage devices due to their relatively higher energy density.[1,2] LIBs find many uses in a variety of applications, such as portable electronics, electric and hybrid electric vehicles, and stationary energy storage systems, as well as others. Compared with LIBs, sodium-ion batteries have recently attracted much attention as an alternative to LIBs for electric energy storage applications owing to the low cost and abundant sodium resources.[3] Aluminum ion batteries are promising alternatives due to their advantages of low cost, nontoxic nature, and earth abundance as well as the three electron redox couples that provide a competitive storage capacity compared to the single-electron, lithium-ion storage.[4,5] The traditional LIBs with organic liquid electrolytes have some drawbacks such as safety issues and low-energy density. However, solid-state Li batteries are expected to use metallic Li anodes due to the use of non-flammable solid electrolytes, which enable a significant increase in energy density. The introduction of metal anodes makes solid-state batteries (SSBs) promising for next-generation high energy density batteries. Particularly, lithium metal has a high theoretical specific capacity (3860 mAh g^{-1}), low-density (0.53 g cm^{-3}), and the lowest electrochemical potential (~3.04 V vs. standard hydrogen electrode (SHE)). Compared to liquid electrolyte-based Li-ion batteries, SSBs are believed to be safer, have longer life cycles, higher energy density, and fewer packaging requirements.[6–12] Therefore, SSBs have received considerable attention during the last decades.

In this short review, we briefly describe the advances in solid-state Li, Na, and Al batteries as well as the existing challenges while also proposing several possible research directions for circumventing the challenges.

Fundamentals of Solid Electrolytes in Solid-State Batteries

Theory of Ion Conduction in Solid-State Electrolytes

For the inorganic solid electrolyte, ionic conduction follows the Arrhenius temperature dependence (**Equation 1**):

$$\sigma_i = \frac{A}{T}\exp[-\frac{E_a}{kT}] \tag{1}$$

where σ_i denotes ionic conductivity, A represents the pre-exponential factor, T signifies the absolute temperature (in kelvins), E_a is the activation energy, and k is the Boltzmann constant.

To calculate the mobility of the charge carrier, use **Equation 2**:

$$\mu = \frac{qD}{kT} \tag{2}$$

In this equation, q represents the carrier charge, D denotes the diffusion coefficient of metal ions, k is the Boltzmann constant, and T is the absolute temperature.[13] The motion of a single particle jumping from an occupied site to an adjacent energetically equivalent unoccupied site may be described by a random-walk theory.[14]

The relationship between the conductivity and the diffusion coefficient follows the Nernest-Einstein Equation (**Equation 3**):

$$\sigma_i = \frac{N_c q^2 D}{kT} \tag{3}$$

where N_c is the number of mobile ions. The ionic conductivity is proportional to the N_c and D.

For polymer electrolytes, the ionic conductivity usually follows the Arrhenius or Vogel-Tammann-Fulcher (VTF) equations or both of them together.[15] Usually, the VTF behavior seems more suitable for the solid polymer electrolytes, as described by **Equation 4**

$$\sigma_t = \sigma_0 T^{-\frac{1}{2}}\exp[-\frac{B}{T-T_0}] \tag{4}$$

where **B** is the pseudo-activation energy of the conductivity, and T_0 is the reference temperature, which falls typically 10–50 K below the glass transition temperature (T_g). The ionic motion behavior correlates with the long-range motions of the polymer segments.

Effective media theories describe the conductivity of composite electrolyte materials consisting of a conducting and an insulating phase.[16]

Structures and Electrochemical Processes of Solid-State Li Batteries

Figure 1 schematically shows the structure of an all-solid-state battery. The battery consists of a cathode, a solid electrolyte (M^{n+} ion conductors, M=Li, Na, Al), an anode, and current collectors. The solid electrolyte serves as both an ionic conductor and separator in the SSBs. The electrodes are attached to both sides of the electrolyte. Solid-state batteries need fewer requirements on packaging and thus may reduce the fabrication cost. M^{n+} ions deintercalated from the anode during discharge are transported to the cathode via the solid electrolyte, while the electrons pass through the external circuit powering a device. During the charge/discharge processes, the potential for reactions and strain forming to occur in the electrodes may cause interfacial delamination. This phenomenon is detrimental to the cycling stability of the cells. In general, the utilization of surface modification techniques such as ball-milling, PLD-coating, and softening glassing methods, form the intimate interfacial contact between electrode and electrolyte.[6]

Progress on Solid-State Lithium Batteries

Solid lithium electrolytes (fast Li-ion conductors) constitute an essential component for rechargeable solid-state Li batteries. Generally, solid electrolytes should have high s_i, negligible s_e, a wide voltage window, chemical compatibility with the electrodes, and low costs. Several kinds of electrolytes such as Li_3N, LiPON, Li_2S-based glass, NASICON-type oxides $Li_{1+x}Al_xTi_{2-x}(PO_4)_3$ (LATP), garnet $Li_7La_3Zr_2O_{12}$ (LLZO), perovskite $Li_{0.05-3x}La_{0.5+x}TiO_3$, anti-perovskites $Li_3OCl_{0.5}Br_{0.5}$, and polymer electrolytes, have been studied for their good Li-ion conductivity.[6] The inorganic electrolytes are usually too hard and brittle for flexible battery applications. However, the mechanical strength of polymer
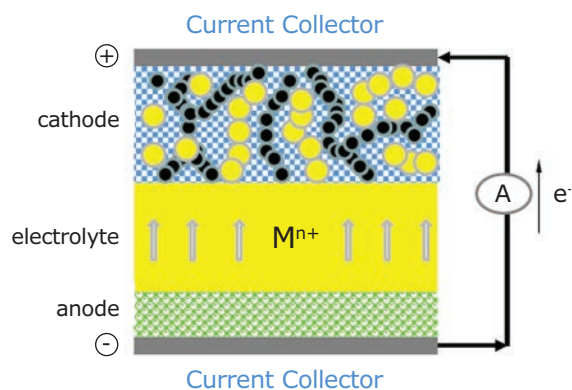
electrolytes is not satisfactory. To solve the problems facing inorganic solid and polymer electrolytes, hybrid electrolyte consisting of a polymer matrix and inorganic filler materials usually have the merits of both of them.

We prepared a garnet, $Li_7La_3Zr_2O_{12}$-based, hybrid solid electrolyte (HSE) membrane consisting of LLZO particles and poly(vinylidene fluoride-*co*-hexafluoropropylene) (PVDF–HFP) polymer matrix for high-performance solid-state lithium batteries for the first time.[8] The HSE membrane exhibited high ionic conductivity, wide electrochemical windows up to ~5.3 V vs. Li+/Li, and excellent flexibility (**Figure 2A–C**). The solid-state lithium battery with this HSE membrane, Li metal anode, and the $LiFePO_4$ cathode showed an initial reversible discharge capacity of 120 mAh g^{-1} at 0.5 C current density at room temperature. The cell showed a capacity retention of 92.5 % at 0.5C after 180 cycles (**Figure 3C**).

Besides developing the solid electrolytes with high ionic conductivity, improving the cyclability of metal batteries requires the stabilization of the metal anode. We reported an organic and inorganic composite membrane (CPM) composed of PVDF-HFP and LLZO particles to protect the Li anode.[17] The CPM-modified Li symmetric cell showed no apparent voltage hysteresis over 500 h at 2 mA cm^{-2}. Moreover, the CPM modified Li|LFP cell can stably run 800 cycles at 1C and retain a high average Coulombic efficiency of ~99.95%. We also found that the composite electrolyte membranes consisting of polyacrylonitrile (PAN)-$Li_{6.5}La_3Zr_{1.5}Ta_{0.5}O_{12}$ (LLZTO) matrix as well as dual salts $LiClO_4$ and $Mg(ClO_4)_2$ can improve the cycling stability of the lithium battery.[18] We found another notable feature worth to noting that the magnesium salt is favorable for facilitating the
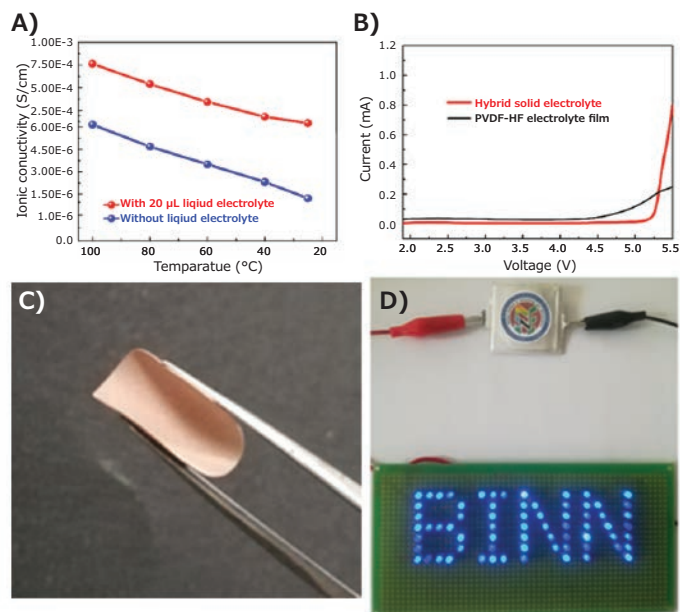

Figure 2. A) Temperature dependence of the Li+ ion conductivity of the HSE membranes free of and infiltrated with 20mL liquid electrolyte, respectively. B) Comparison of linear sweep voltammograms of pure PVDF-HFP electrolyte and the HSE. C) Photograph of the HSE membrane in a bent state, D) Photograph of a LED screen showing the letters of BINN, powered by the flexible pouch cell with this hybrid electrolyte. Reproduced with permission from reference 8, copyright 2018 Elsevier Ltd.
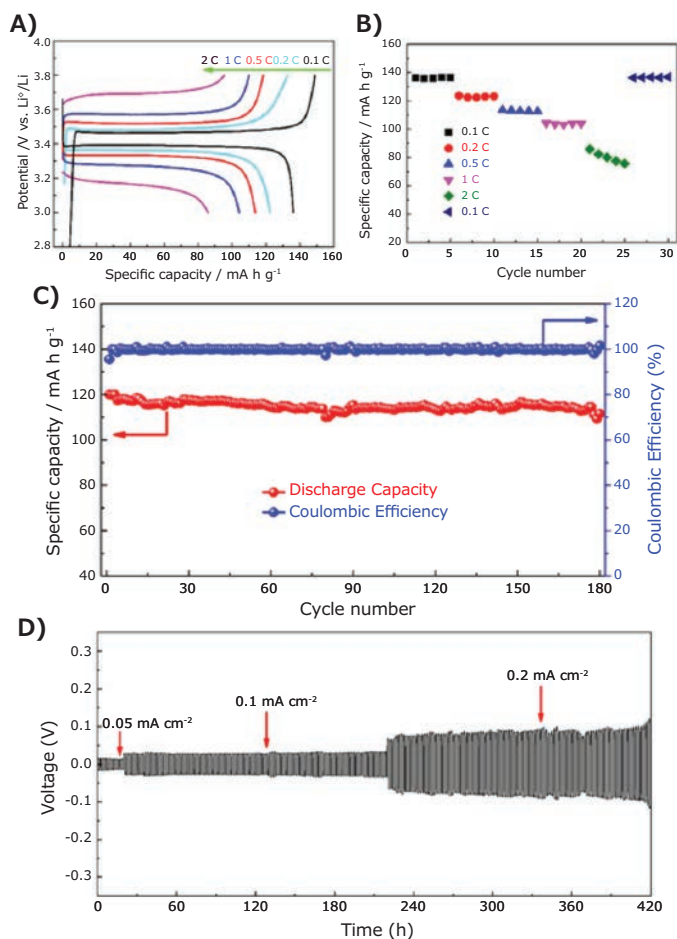

Figure 1. Schematic illustration of a solid-state battery based on M^{n+} ion conduction. Reproduced with permission from reference 6, copyright 2017 Elsevier.

Figure 3. A) The first charge/discharge curves of the solid-state lithium battery at various current densities. **B)** Rate performance of the solid-state lithium battery in a potential range of 3.0–3.8 V vs. Li+/Li tested at 25 °C. (c) Cyclability performance tested at 0.5C rate. **D)** Voltage profile of the lithium plating/stripping cycling in the symmetrical Li|HSE|Li cell at 0.05, 0.1, and 0.2 mA cm-2, respectively. Reproduced with permission from reference 8, copyright 2018 Elsevier Ltd.

decomposition of $LiPF_6$ in the electrolyte to produce fluoride ions. Thus, a stable, protective layer of magnesium fluoride forms on the surface of the lithium anode, which can effectively inhibit the growth of lithium dendrites and increase the cycle life of the battery.

Further research to improve the rate performance of solid-state lithium batteries, using the ion-conducting polymer matrix as a binder in preparing the cathode or coating the cathode particles with ion-conducting materials is needed. In addition, a stabilizing lithium metal anode is also necessary to improve the cyclability of solid-state lithium batteries.

Progress on Solid-State Sodium Batteries

Solid-state sodium batteries have many merits, such as high-energy density, high safety, and serving as an abundant resource of sodium. The investigated solid-state electrolytes include b-alumina ($Na_2O\cdot11Al_2O_3$), $Na_3Zr_2Si_2PO_{12}$, $Na_3P_{1-x}As_xS_4$ ($0 \leq x \leq 0.5$) Na_3PSe_4, $94Na_3PS_4\text{-}6Na_4SiS_4$, Na_3SbS_4, $50Na_2S\text{-}50P_2S_5$, $60Na_2S\text{-}40GeS_2$, $50Na_2S\text{-}50SiS_2$, and others.[19] However, low conductivity of solid electrolytes, as well as the high

interfacial resistance between electrolyte and electrodes, present two main challenges for practical application of solid-state sodium batteries. To address the low conductivity of solid electrolyte of $Na_3Zr_2Si_2PO_{12}$ (NZSP) at room temperature, we prepared NaSICON structured Ca^{2+}-doped $Na_3Zr_2Si_2PO_{12}$ with a higher ionic conductivity of 1.67×10^{-3} S cm-1 at room temperature.[10] Neutron powder diffraction experiments (NPD) unveiled the anisotropic thermal displacements of the Na atoms and a more rigid framework structure by Ca^{2+} substitution for Zr^{4+} in NZSP, which is favorable for Na diffusion.

Researchers developed a robust, Ca-doped, NZSP-type monolithic architecture to solve the poor interfacial contact between electrodes and electrolytes. The capacity of the monolithic solid-state battery with sodium metal anode and $Na_3V_2(PO_4)_3$ cathode maintained 94.9 mAh g-1 at 1 C after 450 cycles (**Figure 4C**). Also, it showed a high rate capability and excellent cyclability. This unique design of monolithic electrolyte architecture provides a promising approach to achieve high-performance solid-state sodium batteries.

Current findings illustrate the need for scaling up the process of monolithic batteries as a key technology in future research. In addition, stabilizing metal Na anodes is a crucial technology to improve the cyclability of solid-state sodium batteries.

Progress on Solid-State Aluminum Batteries

Aluminum (Al) has many merits; it is abundantly available, lightweight, and has three electrons per atom Al. Allowing the achievement of the theoretical specific capacity of 2980 mAh g-1 and a volume capacity of 8046 Ah L-1.[4,5] However, the development of an Al battery is hurdled by a solid electrolyte with high Al^{3+} conductivity. We identified the Al diffusion mechanism in $(Al_{0.2}Zr_{0.8})_{20/19}Nb(PO_4)_3$ through high-temperature NPD experiments and atomic-resolution scanning transmission electron microscopy (STEM) analyses.[11] Temperature-driven Al displacement suggests that Al^{3+} ions diffuse across the structure by a vacancy mechanism. **Figure 5A** shows a Z-contrast (Z: atomic number) atomic-resolution high-angle annular dark-field (HAADF) image of $(Al_{0.2}Zr_{0.8})_{20/19}Nb(PO_4)_3$ taken along the [010] zone-axis. The yellow arrows indicate Al^{3+} ion columns, identified in the {10-2} crystallographic planes. **Figure 5B** presents the intensity profile of the Al^{3+} ion columns along a dash-dot line A-B in **Figure 5A**. The variation of the intensity of the Al^{3+} site suggests a random distribution of Al^{3+} and vacancies, promoting Al^{3+} transport in the ionic channel. Moreover, we first reported a rechargeable solid-state Al battery assembled with V_2O_5 nanorods/rGO (reduced graphene oxide) as a cathode, a dense $(Al_{0.2}Zr_{0.8})_{20/19}Nb(PO_4)_3$ pellet as an electrolyte and Al as the anode. The addition of a small amount of the molten-salt electrolyte consisting of sodium chloride (99.99%) and aluminum chloride (99.9%) (1:1.63 in mole ratio) improved Al^{3+} ion diffusion in the cathode/electrolyte interface. As shown in **Figure 5F**, the first discharge specific capacity of the cell reached 7.5 mAh g-1 at 120 °C while the charge specific capacity was 6.5 mAh g-1. Increasing the temperature to 150 °C, the cell showed a capacity value of ~10 mAh g-1.
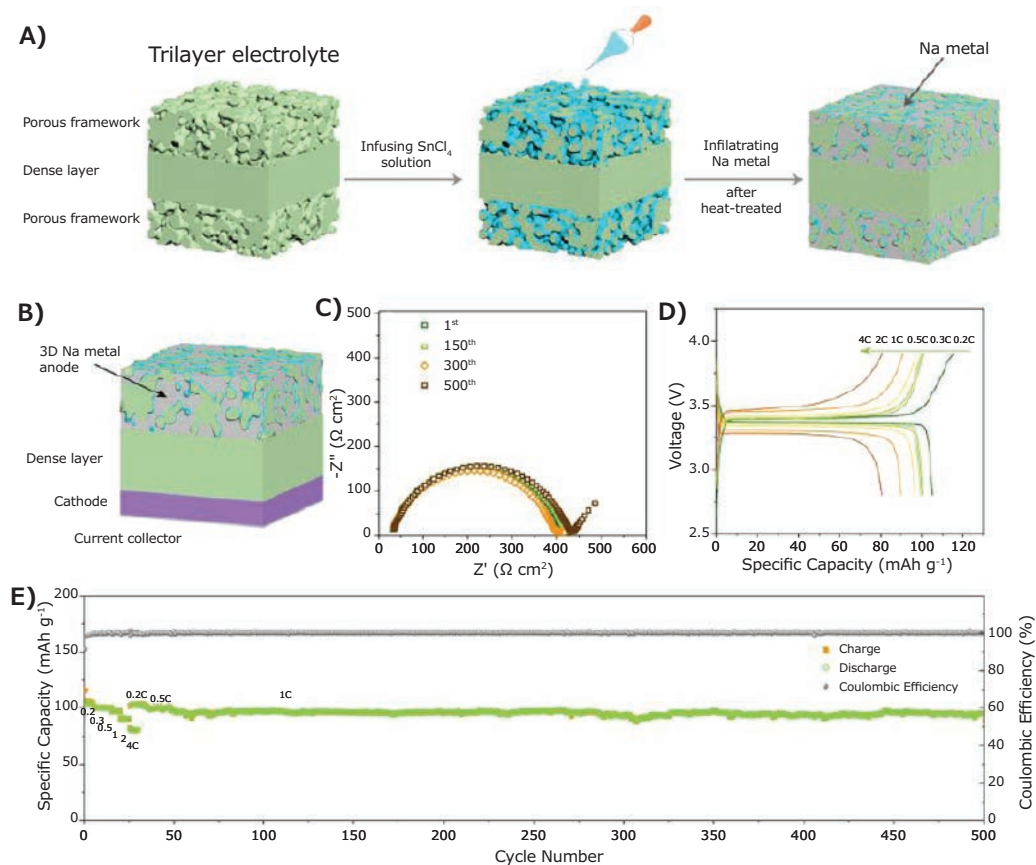
Figure 4. A) Schematic illustration of the monolithic NZSP solid-state electrolyte. B) Schematic of the full SSB. (c~e) Electrochemical performance of the solid-state sodium battery. Reproduced with permission from reference 10, copyright 2019 Wiley-VCH.
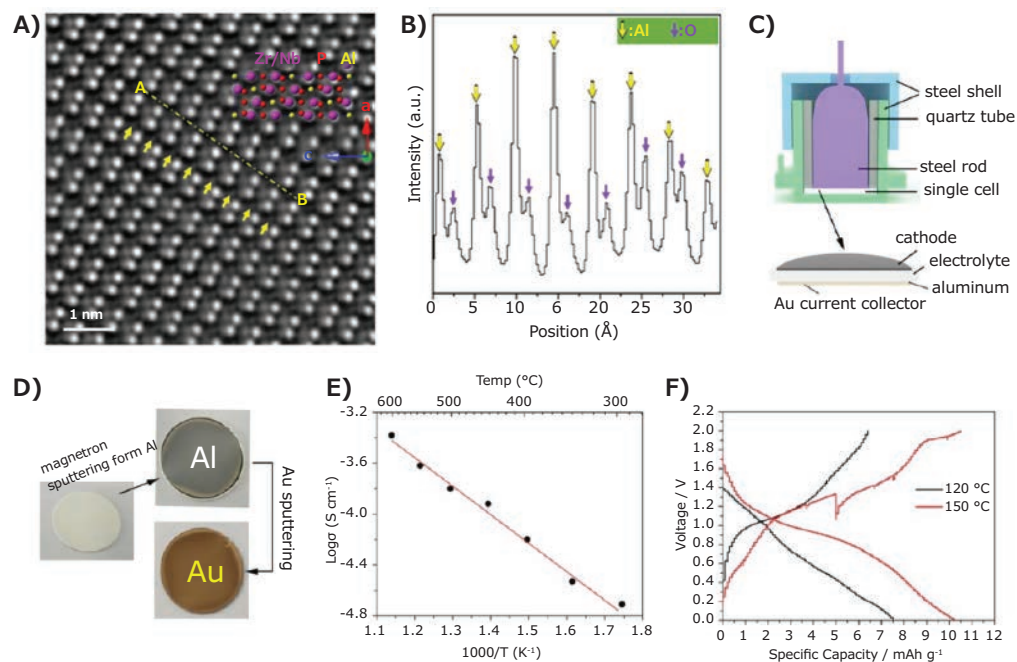

Figure 5. A,B) STEM images of $(Al_{0.2}Zr_{0.8})_{20/19}Nb(PO_4)_3$. C) Schematic diagram of the Swagelok cell used for electrochemical tests. D) The preparation process of Al anode. E) Temperature dependence of the Al^{3+} ion conductivity of $(Al_{0.2}Zr_{0.8})_{20/19}Nb(PO_4)_3$. F) The first discharge-charge curves of the solid-state V_2O_5 nanorods/rGO|Al battery tested at 2 mA g^{-1} at 120 °C and 150 °C, respectively. Reproduced with permission from reference 11, copyright 2018 Chinese Physical Society and IOP Publishing Ltd.

The urgent need for solid electrolytes with high ionic conductivities for solid-state Al batteries demands future research. The effective interfacial contact between electrolyte and electrode are also necessary to achieve high-performance batteries.

Scientists have studied solid-state batteries with other ion-conducting electrolytes previously. Magnesium (Mg) batteries present another promising alternative to overcome the issues of poor safety and low energy density faced by LIBs. However, the development of a magnesium battery is plagued by the poor Mg^{2+} mobility in solids. Ceder et al. first reported fast Mg^{2+} ion conduction in spinel $MgSc_2Se_4$ by *ab initio* calculation and experimental characterization, which can integrate with Mg cathodes, like spinel-$MgTi_2S_4$ and Chevrel-Mo_6S_8, to make solid-state magnesium batteries.[20] Their theoretical calculation also predicted that other chalcogenide spinels might have high Mg^{2+} mobility.

Conclusion and Perspective

In summary, due to safety concerns, solid-state batteries have drawn considerable attention in recent years. Although the scientific community has achieved a great deal of progress on the solid-state Li batteries during the past decades, the low ionic conductivity of solid electrolytes and poor interfacial contact between electrolyte and electrodes fall among the two main challenges researchers still face. Solid-state Na and Al batteries are emerging technologies since they have advantages in terms of low costs and high volumetric-energy densities, respectively, compared to Li batteries. The author of this review provided an overview of the progress of solid-state Li, Na, and Al batteries developed in our lab. For solid-state batteries, solid electrolytes are the key components.

Developing solid electrolytes with high ionic conductivity becomes highly desirable. Achieving and maintaining good contact between solid electrodes and solid electrolytes proves essential for reducing the interfacial resistance. Utilizing soft polymer interlayer, a small amount of gel or liquid electrolytes has proven as feasible approaches to improve the ionic transport in the interfaces. Additionally, researchers may employ additional strategies to improve cathode performance. For example, scientists may use the ion-conducting polymer matrix as a binder in preparing the cathode or coating the cathode particles with ion-conducting materials, e.g., $LiNbO_3$ and $Li_{1+x}Al_xTi_{2-x}(PO_4)_3$ by wet chemical methods.

Moreover, metal anode protection has proven vital for achieving long-term stability of solid-state batteries. In particular, solid electrolyte interphase (SEI) film-forming additives and artificial SEI offer feasible strategies to suppress Li dendrites and improve the long-term stability of lithium batteries. Combining experimental and theoretical calculation approaches enables one to reveal the interface evolution during charge-discharge cycles and thus improve the performances of solid-state batteries. It still takes some time to commercialize the solid-state batteries.

Acknowledgments

References

(1) Tarascon, J. M.; Armand, M. *Nature* **2001**, *414*, 359–367.
(2) Goodenough, J. B.; Kim, Y. *Chem. Mater.* **2010**, *22*, 583–603.
(3) Hou, H. D.; Gan, B. H.; Gong, Y. D.; Chen, N.; Sun, C. W. *Inorg. Chem.* **2016**, *55*, 9033–9037.
(4) Elia, G. A.; Marquardt, K.; Hoeppner, K.; Fantini, S.; Lin, R.Y.; Knipping, E.; Peters, W.; Drillet, J. F.; Passerini, S.; Hahn, R. *Adv. Mater.* **2016**, *28*, 7564–7579.
(5) Ambroz, F.; Macdonald, T. J.; Nann, T. *Adv. Energy Mater.* **2017**, *7*, 1602093.
(6) Sun, C. W.; Liu, J.; Gong, Y. D.; Wilkinson, D. P.; Zhang, J. J. *Nano Energy* **2017**, *33*, 363–386.
(7) Hou, H. D.; Xu, Q. K.; Pang, Y. K.; Wang, J. L.; Zhang, C.; Sun, C. W. *Adv. Sci.* **2017**, *4*, 1700072.
(8) Zhang, W. Q.; Nie, J. H.; Li, F.; Wang, Z. L.; Sun, C. W. *Nano Energy* **2018**, *45*, 413–419.
(9) Ban, X. Y.; Zhang, W. Q.; Chen, N.; Sun, C. W. *J. Phys. Chem. C* **2018**, *122*, 9852–9858.
(10) Lu, Y.; Alonso, J. A.; Yi, Q.; Lu, L.; Wang, Z. L.; Sun, C. W. *Adv. Energy Mater.* **2019**, *9*, 1901205.
(11) Wang, J.; Sun, C. W.; Gong, Y. D.; Zhang, H. R.; Alonso, J. A.; Fernández-Díaz, M. T.; Wang, Z. L.; Goodenough, J. B. *Chin. Phys. B* **2018**, *27*, 128201.
(12) Zhang, Y.; Lai, J. Y.; Gong, Y. D.; Hu, Y. M.; Liu, J.; Sun, C. W.; Wang, Z. L. *ACS Appl. Mater. Interfaces* **2016**, *8*, 34309–34316.
(13) Sorensen, O. T. *Nonstoichiometric Oxides*, Academic Press, INC., New York, **1981**.
(14) Goodenough, J. B. *Mater. Sci. Forum* **1986**, *7*, 1.
(15) Quartarone, E.; Mustarelli, P. *Chem. Soc. Rev.* **2011**, *40*, 2525–2540.
(16) Bruggeman, D. A. G. *Ann. Phys. (Leipzig)* **1935**, *24*, 636–664.
(17) Zhang, W. Q.; Yi, Q.; Li, S. Y.; Sun, C. W. *J. Power Sources* **2020**, *450*, DOI: 10.1016/j.jpowsour.2020.227710.
(18) Qiu, G. R.; Sun, C. W. *New J. Chem.* **2020**, *44*, 1817–1824.
(19) Hayashi, A.; Masuzawa, N.; Tsuji, F.; Hotehama, C.; Sakuda, A.; Tatsumisago, M. *Nat. Commun.* **2019**, *10*, 5266.
(20) Canepa, P.; Bo, S.; Gautam, G. S.; Key, B.; Richards, W. D.; Shi, T.; Tian, Y.; Wang, Y.; Li, J.; Ceder, G. *Nat. Commun.* **2017**, *8*, 1759.
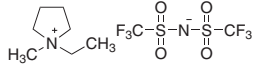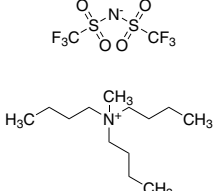
Electrolyte Solutions

Lithium Hexafluorophosphate Solutions, Battery Grade: H_2O <15 ppm; HF <50 ppm; APHA <50.

Name	Specifications	Cat. No.
1.0 M LiPF$_6$ in EC/DMC=50/50 (v/v)	in ethylene carbonate and dimethyl carbonate	**746711-100ML** **746711-500ML**
1.0 M LiPF$_6$ in EC/EMC=50/50 (v/v)	in ethylene carbonate and ethyl methyl carbonate	**746738-100ML** **746738-500ML**
1.0 M LiPF$_6$ in EC/DEC=50/50 (v/v)	in ethylene carbonate and diethyl carbonate	**746746-100ML** **746746-500ML-A**
1.0 M LiPF$_6$ in DMC	in dimethyl carbonate	**746754-100™L** **746754-500ML-A**
1.0 M LiPF$_6$ in EMC	in ethyl methyl carbonate	**746762-100ML** **746762-500ML**

Name	Specifications	Cat. No.
1.0 M LiPF$_6$ in DEC	in diethyl carbonate	**746770-100ML** **746770-500ML**
1.0 M LiPF$_6$ in PC	in propylene carbonate	**746789-100ML** **746789-500ML**
2.0 M LiPF$_6$ EC/DEC=50/50(v/v)	in ethylene carbonate and diethyl carbonate	**809349-100ML** **809349-500ML**
2.0 M LiPF$_6$ in EC/DMC=50/50(v/v)	in ethylene carbonate and dimethyl carbonate	**809357-100ML** **809357-500ML**
2.0 M LiPF$_6$ EMC	in ethylmethyl carbonate	**809403-100ML** **809403-500ML**
2.0 M LiPF$_6$ DMC	in dimethyl carbonate	**809411-100ML** **809411-500ML**
2.0 M LiPF$_6$ PC	in propylene carbonate	**809470-100ML** **809470-500ML**
2.0 M LiPF$_6$ EC/EMC=50/50(v/v)	in ethylene carbonate and ethylmethyl carbonate	**809365-100ML** **809365-500ML**
2.0 M LiPF$_6$ DEC	in diethyl carbonate	**809543-100ML** **809543-500ML**

Ionic Liquids

Name	Structure	Purity	Cat. No.
1-Butyl-2,3-dimethylimidazolium bis(trifluoromethylsulfonyl)imide		≥99%	**900804-25G**
1-Butyl-3-methylimidazolium bis(trifluoromethylsulfonyl)imide		≥99%	**900802-25G**
1-Butyl-3-methylimidazolium chloride		≥99%	**900856-25G**
1-Butyl-1-methylpiperidinium bis(trifluoromethylsulfonyl)imide		≥99%	**900807-25G**
1-Butyl-1-methylpyrrolidinium bis(trifluoromethylsulfonyl)imide		>99%	**900873-25G**
Diethyl carbonate, H$_2$O <10 ppm acid <10 ppm		≥99%	**900018-25G** **900018-500G**
1-Ethyl-3-methylimidazolium acetate		≥98%	**900787-25G**
1-Ethyl-3-methylimidazolium bis(trifluoromethylsulfonyl)imide		≥99%	**900801-25G**
1-Ethyl-3-methylimidazolium chloride		>99%	**900771-25G**
1-Ethyl-3-methylimidazolium hexafluorophosphate		≥99%	**900779-25G**
1-Ethyl-3-methylimidazolium tetrafluoroborate		≥99%	**900772-25G**

Name	Structure	Purity	Cat. No.
1-Ethyl-1-methylpyrrolidinium bis(trifluoromethylsulfonyl)imide		≥99%	**900813-25G**
1-Methyl-1-propylpiperidinium bis(trifluoromethylsulfonyl)imide		≥99%	**900806-25G**
Tributylmethylammonium bis(trifluoromethylsulfonyl)imide		≥99%	**900857-25G**

Electrolyte Materials

Name	Composition	Purity	Cat. No.
Lithium bis(oxalato)borate	$LiB(C_2O_4)_2$	-	**757136-25G**
Lithium difluoro(oxalato)borate	$LiBF_2(C_2O_4)$	-	**774138-25G**
Lithium hexafluoroarsenate(V)	$LiAsF_6$	98%	**308315-10G**
Lithium hexafluorophosphate	$LiPF_6$	≥99.99% trace metals basis	**450227-5G** **450227-25G** **450227-250G**
Lithium perchlorate	$LiClO_4$	99.99% trace metals basis	**634565-10G** **634565-100G**
Lithium phosphate monobasic	LiH_2PO_4	99%	**442682-500G-A**
Lithium tetrafluoroborate	$LiBF_4$	99.99% trace metals basis	**451622-5G** **451622-25G**
Lithium trifluoromethanesulfonate	CF_3SO_3Li	99.995% trace metals basis	**481548-5G** **481548-25G**
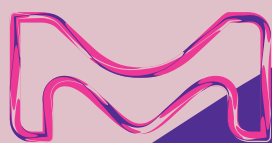
MID-CAREER RESEARCHER AWARD

The Mid-Career Researcher Award recognizes exceptional achievements in materials research made by mid-career professionals. It is not limited to the method of characterization or the class of materials observed. (MRS acknowledges the generosity of Merck for endowing this award.)
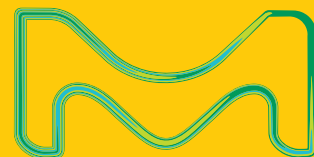
Xiangfeng Duan

University of California, Los Angeles

For contributions to rational design and assembly of layered materials for electronic, photonic and energy devices

Van der Waals Heterostructures from 2D Materials and Beyond
The heterogeneous integration of dissimilar materials is a long pursuit of the materials science community and has defined the material foundation for modern electronics and optoelectronics. The typical material integration approaches usually involve strong chemical bonds and aggressive synthetic conditions, and are often limited to materials with strict structure match and processing compatibility.

Professor Duan will discuss the exploration of the van der Waals force for bond-free integration of highly disparate materials without lattice and processing limitations, thus producing a new generation of artificial heterostructureswith an atomically clean interface and electronic structure by design to unlock new physical limits and enable high-performance devices beyond the reach of existing material systems at an upcoming MRS event.

The life science business of Merck operates as MilliporeSigma
in the U.S. and Canada.

MERCK